AGU PUBLICATIONS

JGR

Journal of Geophysical Research: Atmospheres

RESEARCH ARTICLE

10.1002/2013JD020217

Key Points:
- Cross-correlation algorithm for continuously sampled DITF data
- Quasi 3-D conversion of 2-D interferometric maps of lightning
- Measured 3-D velocities of K-events as a function of time

Supporting Information:
- Flash animation

Correspondence to:
M. G. Stock,
mike@lightning-interferometry.com

Citation:
Stock, M. G., M. Akita, P. R. Krehbiel, W. Rison, H. E. Edens, Z. Kawasaki, and M. A. Stanley (2014), Continuous broadband digital interferometry of lightning using a generalized cross-correlation algorithm, *J. Geophys. Res. Atmos.*, *119*, doi:10.1002/2013JD020217.

Received 17 MAY 2013
Accepted 18 FEB 2014
Accepted article online 23 FEB 2014

Continuous broadband digital interferometry of lightning using a generalized cross-correlation algorithm

M. G. Stock[1], M. Akita[1,2], P. R. Krehbiel[1], W. Rison[1], H. E. Edens[1], Z. Kawasaki[2], and M. A. Stanley[1]

[1]Langmuir Laboratory, New Mexico Institute of Mining and Technology, Socorro, New Mexico, USA, [2]Department of Information and Communications Technology, Graduate School of Engineering, Osaka University, Suita, Japan

Abstract The VHF Broadband Digital Interferometer developed by Osaka University has been improved to allow continuous sampling over the entire duration of a lightning flash and to utilize a generalized cross-correlation technique for determining the lightning source directions. Time series waveforms of 20–80 MHz signals received at three orthogonally located antennas are continuously digitized over multisecond intervals, as opposed to sequences of short-duration triggers. Because of the coherent nature of the measurements, radiation sources are located down into the ambient receiver and environmental noise levels, providing a quantum leap in the ability to study lightning discharge processes. When postprocessed using cross correlation, the measurements provide angular uncertainties less than 1° and time resolution better than 1 μs. Special techniques have been developed to distinguish between actual lightning sources and noise events, with the result being that on the order of 50,000–80,000 radiation sources are located for a typical lightning flash. In this study, two-dimensional interferometer observations of a classic bilevel intracloud flash are presented and combined with three-dimensional Lightning Mapping Array observations to produce a quasi 3-D map of lightning activity with the time resolution of the interferometer. As an example of the scientific utility of the observations, results are presented for the 3-D progression speed of negative leaders associated with intracloud K-leaders.

1. Introduction

Lightning discharges produce electromagnetic radiation over a broad spectrum of radio frequencies, extending from the ULF through UHF and higher. VLF/LF sferics sense impulsive current events such as those produced by cloud-to-ground strikes and some in-cloud processes and are commonly used to locate where lightning strikes ground [e.g., *Cummins et al.*, 1998] and, increasingly, the locations of in-cloud events [e.g., *Schultz et al.*, 2011]. VHF radiation (30–300 MHz) senses the smaller-scale breakdown activity itself and can be used to map the detailed development of individual flashes within storms.

VHF lightning mapping has traditionally been done in one of two ways: (a) by using interferometric techniques to determine the direction of arrival of the radiation [e.g., *Warwick et al.*, 1979; *Hayenga*, 1984; *Richard et al.*, 1986; *Rhodes et al.*, 1994; *Shao et al.*, 1996; *Ushio et al.*, 1997; *Kawasaki et al.*, 2000; *Cao et al.*, 2010] or (b) by using time of arrival (TOA) measurements to image the lightning in three dimensions [e.g., *Proctor*, 1981; *Maier et al.*, 1995; *Rison et al.*, 1999; *Thomas et al.*, 2004]. TOA systems accurately measure the arrival times of impulsive VHF events at a number of ground locations, usually widely spaced over distances of kilometers to tens of kilometers. For the New Mexico Tech Lightning Mapping Array (LMA), the timing uncertainty is empirically found to be about 30 ns RMS, corresponding to source location accuracies as good as 10 m RMS over the network [*Thomas et al.*, 2004]. Although the VHF radiation is incoherently detected at each station, the TOA values are coherently combined to produce detailed three-dimensional observations of the spatial and temporal development of individual flashes. Up to a thousand or more impulsive sources are typically located for large flashes, in time resolution windows of 80 μs or 10 μs duration. With current technology, real-time processing is possible for data decimated to successive 400 μs windows.

Interferometer systems receive the VHF signals coherently at an array of closely spaced antennas, typically a few wavelengths apart (10–20 m or so), and obtain one- or two-dimensional directions of arrival of the lightning radiation sources. The signals from pairs of sensing antennas are coherently correlated to accurately determine the phase or time difference of arrival of the two signals and hence the angle cosines of the source direction. Measurements along two orthogonal baselines can be used to determine the spherical angles of sources and thereby their azimuth and elevation angles.

Initial interferometric lightning studies (as well as early radio astronomy studies) utilized narrowband systems, i.e., systems whose receiving bandwidth B is small compared to the center frequency f_c. The coherent interference was determined at first using analog multipliers ("mixers") and quadrature phase detection techniques to determine the phase difference of arrival ϕ at the two antennas, time-averaged, and then digitized or otherwise recorded at then-available rates. Because the measurements were narrowband, multiple baseline lengths were required to obtain the desired angular resolution and to resolve the fringe ambiguities of the measurements [e.g., *Warwick et al.*, 1979; *Shao*, 1993; *Rhodes et al.*, 1994], requiring an increased number of antennas and receiving channels.

The narrowband restriction was primarily technological, as high-speed digitizers and increasingly fast computers now currently available allow the raw time series data to be directly recorded for subsequent processing with advanced Fourier spectral techniques. Broadband time series waveforms of the VHF signals from as few as three receiving antennas can be digitized and stored for detailed postprocessing. The signals from pairs of antennas are analyzed digitally using Fourier techniques to obtain the amplitude and phase of their cross-spectrum $S_{xy}(f)$ in the frequency domain, from which the phase difference versus frequency is obtained. Linear fits of the slope of $\phi(f)$ correspond to the time differences of arrival at the two antennas. The broadbanding provides a wide range of baseline lengths (in terms of wavelengths) that automatically resolves the fringe ambiguities of narrowband measurements [*Shao et al.*, 1996; *Ushio et al.*, 1997; *Kawasaki et al.*, 2000; *Cao et al.*, 2010].

In this study we report on the development of a broadband lightning interferometer that obtains the arrival directions using a generalized cross-correlation technique and does so continuously for entire flashes. The correlation technique carries the phase versus frequency approach one step further by taking the inverse Fourier transform of the cross spectrum to obtain the cross-correlation function $R_{xy}(\tau)$ in the time domain. The cross correlation is "generalized" by the use of windowing functions that emphasize particular features of the data. When applied to broadband measurements, the time differences of arrival at pairs of antennas can be accurately determined from the peak of the cross-correlation function, parabolically interpreted to more accurately define the peak. The basic approach is very similar to that recently reported on by *Sun et al.* [2012] and has been developed in parallel with and independently of their study. In both instances, the analyses utilize special techniques developed for correlation analyses in general.

The platform used in this study has been the Osaka University Broadband Digital Interferometer, or DITF [*Ushio et al.*, 1997; *Kawasaki et al.*, 2000]. The DITF was operated at Langmuir Laboratory during the summers of 2011 and 2012 for the purpose of combining its measurements with those of the Langmuir Lightning Mapping Array (LMA), a TOA system that provides 3-D observations of flashes [*Rison et al.*, 1999; *Thomas et al.*, 2004]. As discussed below and in a companion study by M. Akita et al. (Data processing procedure using distribution of slopes of phase differences for broadband VHF interferometer, submitted to *Journal of Geophysical Research*, 2013), the original recording system of the DITF was upgraded with high-speed streaming digitizers capable of recording continuous data for entire flashes with a large (73 dB) dynamic range. The combination of continuous recording and coherent processing has enabled the system to locate radiation events down into the background receiver and environmental noise levels, providing observations of unprecedented sensitivity and detail.

A major part of the study has been applying and developing techniques for analyzing the observations, to extract as much information as possible about the lightning processes and to distinguish between signal events and noise. In addition to describing the techniques, we present observations of a bilevel intracloud lightning discharge that illustrate the substantially greater amount of information about discharge development than has previously been obtained, and how the LMA and interferometer observations valuably complement each other.

2. The Broadband Interferometer

The Osaka University Digital Interferometer consists of three resistively coupled flat plate antennas arranged to form two equal-length orthogonal baselines. A fourth antenna is used to provide triggers for recording the time series data. Due to being resistively coupled, the antennas sense the time derivative of the incident electric field, dE/dt, and hence partially compensate for the falloff of lightning's VHF spectrum with increasing frequency. For the present study, the antenna separation was 10.2 m in the two perpendicular

Table 1. Table of the Parameters for the Interferometer (INTF) and the Lightning Flash

Sensor Parameters		
Number Antennas	3	
Baselines	10.2	m
Bandwidth	60	MHz
Sampling Rate	180	MS s^{-1}
Flash Parameters		
Time	03:08:10.390	UT
INTF sources	62598	
LMA sources	1092	

directions and the received signals were band limited to 20–80 MHz before being digitized. A summary of the interferometer's attributes is given in Table 1.

Due to technology limitations at the time of its original design, the Osaka DITF was restricted to recording only a few milliseconds of high-speed (200 MS s^{-1}, 10 bit) data before needing to output the data to disk. To obtain overviews of entire flashes, it was necessary to record sequences of short-duration (2.56 μs) time windows, triggered when the signal from the fourth antenna exceeded an effective threshold level. Up to 2048 such windows could be recorded before needing to do a data transfer to the host computer. Similar triggering methods are used by other broadband interferometer systems [e.g., *Shao et al.*, 1996; *Qiu et al.*, 2009; *Cao et al.*, 2010; *Sun et al.*, 2012]. To sample an entire flash, the threshold is needed to be set at a relatively high value. The net result, determined during the course of the present study, was that the sequentially sampled DITF observations gave results similar to those produced by low trigger-rate (80 μs time window) LMA time-of-arrival data. Continuously propagating and radiating events such as dartleaders and K-leaders were imaged [*Akita et al.*, 2010] but provided substantially less detail than that obtained by the analog-based but continuous recording, narrowband interferometer developed earlier at NM Tech [*Rhodes et al.*, 1994; *Shao et al.*, 1995; *Shao and Krehbiel*, 1996]. The difference was due in large part to the data being continuously recorded rather than sampled at a low duty-cycle rate.

In anticipation of the difficulties of obtaining the desired observations with the sequential triggering approach, in 2011, we adapted high-speed digitizing capability developed for another research project to implement a continuous recording system that was operated in parallel with the original DITF recording electronics. The parallel system recorded four channels of time-synchronized 16 bit 180 MS s^{-1} data, using PC-based digitizer cards that streamed their data directly into PC memory. Thirty-two Gb of PC memory was sufficiently large to record up to 20 s of time series waveforms before needing to transfer the data to fast solid state disk. The system allowed data to be continuously recorded for entire flashes, either for sets of 2 s duration segments of up to 20 s continuously. Accurate time synchronization with the LMA data was obtained by digitizing the one pulse per second serial output of a GPS receiver on the fourth high-speed channel.

At the same time, we began developing a general cross-correlation technique for processing the data, for comparison with the phase-slope analysis procedure originally developed for the DITF. At this point, it is important to note that the two techniques are basically equivalent to each other, as the Fourier transform of a time-delayed signal $x(t - \tau_d)$ has a phase $\phi(f) = 2\pi f \tau_d$ that increases linearly with frequency. However, by utilizing generalized cross-correlation methods, a wealth of previously developed mathematical techniques can be applied, including but not limited to the estimation of the theoretical angular uncertainty of a broadband interferometer and the use of windowing functions to improve the source location estimation [e.g., *Hassab and Boucher*, 1979; *Boucher and Hassab*, 1981; *Azaria and Hertz*, 1984; *Carter*, 1987; *Moddemeijer*, 1991; *Jacovitti and Scarano*, 1993].

We first present the theoretical background and techniques for obtaining solutions of broadband interferometer data using cross correlation. Then we present results obtained from analysis of a classic bilevel intracloud flash that illustrate the capabilities of continuous measurements. The observations are valuably complemented by three-dimensional LMA observations of the flash structure and temporal development, which are used to expand the interferometer observations to quasi 3-D results. Similar analyses of the same flash using the phase versus frequency slope technique will be discussed in a companion paper (M. Akita et al., submitted manuscript, 2013).

3. The Generalized Cross-Correlation Technique

For a distant signal arriving at two antennas separated by a distance d, and from the simple geometry of Figure 1, the time difference of arrival τ_d and the phase difference $\Delta\phi$ are related to each other and to the

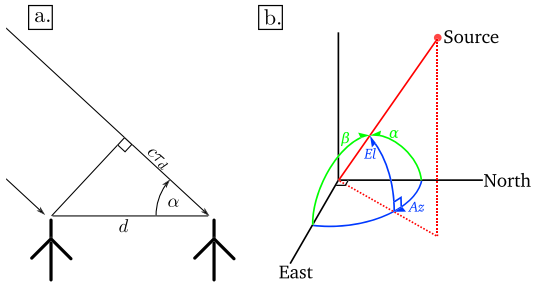

Figure 1. Basic geometry of the interferometer measurements.

angle of incident radiation α according to

$$d\cos\alpha = c\tau_d = \left(\frac{\Delta\phi}{2\pi}\right)\lambda\,, \tag{1}$$

where λ is the wavelength of the radiation and c is the speed of light in air. Measuring the time delay τ_d or the phase difference $\Delta\phi$ determines the direction cosine, $\cos\alpha$, of the source from

$$\cos\alpha = \frac{c\tau_d}{d} = \left(\frac{\Delta\phi}{2\pi}\right)\frac{\lambda}{d}\,. \tag{2}$$

Whereas the direction cosine can be determined directly from correlation measurements of τ_d, its determination from phase values is more complicated due to the 2π ambiguity of phase measurements, necessitating that the phase values versus frequency be "unwrapped" for baselines $d > \lambda/2$. In both cases, however, the estimated value of τ_d cannot exceed the transit time $\tau_{\text{transit}} = (d/c)$ between the two antennas. This physical constraint ensures that the value of $\cos\alpha$ lies in the range ± 1 and is useful in distinguishing between actual sources and random noise events in the correlation measurements.

For sources in located in two spatial dimensions, two angles are needed to specify the direction, requiring an additional measurement for their determination. Equations (1) and (2) still apply, but with the plane tilted to pass through the source location. The second measurement can be obtained from an orthogonal horizontal baseline, which similarly determines the arrival angle β relative to its axis. Letting the two baselines correspond to east and north directions, respectively, and defining the azimuthal angle to increase clockwise from north, we have from spherical trigonometry [e.g., *Rhodes et al.*, 1994] that

$$\begin{aligned}\cos\alpha &= \sin(\text{Az})\cos(\text{El})\\ \cos\beta &= \cos(\text{Az})\cos(\text{El})\,,\end{aligned} \tag{3}$$

where $\cos\alpha$ and $\cos\beta$ are the direction cosines. Geometrically, the above equations correspond to the transformation between unit-radius spherical and Cartesian coordinates, with the spherical angles (θ, ϕ) replaced by their complements (El, Az). The resulting (x, y) coordinates correspond to the direction cosine values $(\cos\alpha, \cos\beta)$. The direction cosines thus represent the projection of the sources from a unit celestial hemisphere down onto the horizontal plane of the antennas [e.g., *Rhodes et al.*, 1994]. The transit time constraint corresponds to $(\cos\alpha)^2 + (\cos\beta)^2 \le 1$, namely to a unit radius circle in the direction cosine plane (e.g., Figure 6b).

The above equations can be inverted to obtain the azimuth and elevation in terms of the two time differences of arrivals, τ_{d1} and τ_{d2}, giving

$$\begin{aligned}\text{Az} &= \arctan\left(\frac{\tau_{d1}}{\tau_{d2}}\right)\\ \text{El} &= \arccos\left(\frac{c}{d}\sqrt{\tau_{d1}^2 + \tau_{d2}^2}\right)\,.\end{aligned} \tag{4}$$

For the case of nonperpendicular baselines that may or may not have a baseline in the north-south direction, these projections can be generalized to

$$\begin{aligned}\text{Az} &= \text{Az}_1 + \arctan\left(\frac{\tau_{d1}\cos(\Delta\theta) - \tau_{d2}}{\tau_{d1}\sin(\Delta\theta)}\right)\\ \text{El} &= \arccos\left(\frac{c}{d}\sqrt{\frac{\tau_{d1}^2 + \tau_{d2}^2 - 2\tau_{d1}\tau_{d2}\cos(\Delta\theta)}{\sin^2(\Delta\theta)}}\right)\,,\end{aligned} \tag{5}$$

where Az_1 is the azimuth angle of baseline 1 and $\Delta\theta = \text{Az}_1 - \text{Az}_2$ is the angle between the baselines.

Estimates of the time delay values can be obtained using the generalized cross correlation. The measured signals at each antenna, x_1 and x_2, are assumed to be band limited and of the form

$$\begin{aligned}x_1(t) &= v(t) + n_1(t)\\ x_2(t) &= v(t - \tau_d) + n_2(t)\,,\end{aligned} \tag{6}$$

where v is the signal from the coherent source and n_1 and n_2 are uncorrelated noise sources. It is particularly important that the signal be band limited consistent with the Nyquist frequency before digitization to eliminate aliasing effects. Otherwise, the effect of aliasing is that the time delay estimate ($\hat{\tau}_d$) will tend to be an integer multiple of the sampling period, which causes the azimuth and elevation solutions to clump [*Moddemeijer*, 1991]. This effect is also seen in data processing using phase-slope analysis, and there is no postprocessing technique that can be used to remove the clumping after the waveforms have been digitized.

If $X_1(f)$ and $X_2(f)$ are the Fourier transforms of x_1 and x_2, then the time delay estimate $\hat{\tau}_d$ can be determined from the maximum value of the cross correlation. The generalized cross correlation makes use of a windowing function in the frequency domain, $W(f)$, which tailors the cross correlation for different purposes. The generalized cross-correlation $R_g(\tau)$ with windowing function $W(f)$ can be found in the following way:

$$x_1(t), x_2(t) \xleftrightarrow{\mathcal{F}} X_1(f), X_2(f)$$
$$\downarrow$$
$$R_g(\tau) \xleftrightarrow{\mathcal{F}} X_1(F)\, X_2^*(f) W(f)\,.$$

Note that a nongeneralized cross-correlation function R_{12} can be determined directly in the time domain by convolving x_1 and x_2, but the computations are prohibitively intensive, and windowing is also more complicated. It is both faster and simpler to utilize fast Fourier transforms to transform into the frequency domain, where the convolution becomes simple multiplication, and then transform back to the time domain.

Numerous windowing functions have been described in the literature. For this study only two windows are considered; no windowing ($W = 1$), and a variation of the Maximum Likelihood windowing function described by *Hassab and Boucher* [1979], W_l, defined as

$$W_l(\omega) = \frac{\Phi_v(\omega)}{\Phi_{n_1}(\omega)\Phi_{n_2}(\omega) + \Phi_v(\omega)\left(\Phi_{n_1}(\omega) + \Phi_{n_2}(\omega)\right)}\,, \tag{7}$$

where Φ_v is the signal spectrum and Φ_n is the noise spectrum. The effect of W_l is to emphasize frequency components that have good signal-to-noise ratio, thereby improving the time delay estimation. The noise spectrum is readily obtained from portions of the record that contain no signal from lightning. The signal spectrum is estimated by differencing the cross spectrum of the current window and the cross spectrum of noise. Estimating Φ_v in this way allows the W_l function to exclude frequency bands contaminated by correlated noise sources.

An estimate of the time difference of a signal arriving at two antennas, $\hat{\tau}_d$, is obtained from the maximum value of the generalized cross-correlation R_g. Because the cross correlation is computed discretely, the maximum of the correlation function is an integer multiple of the sampling period (5.6 ns in this study). To obtain a more accurate value of $\hat{\tau}_d$, the cross spectrum is upsampled before transforming back to the time domain, and a parabola is fit to three upsampled values about the peak [e.g., *Boucher and Hassab*, 1981].

3.1. Implementation

The signals from the antennas are band limited to 20–80 MHz and sampled by a 16 bit, 180 MS s^{-1} PC digitizer that streams the digitized signals into PC memory, allowing for long record lengths. Even though the PC digitizer is capable of streaming the digitized signal into memory indefinitely, the data rates are too fast to transfer selected data segments to hard disk continuously. For this reason the recording is triggered on a flash-by-flash basis, with each trigger making a continuous multisecond record of the VHF time series data (2 s long in the present study). During postprocessing, the records are divided into 256 sample (1.42 μs) windows. Successive windows are overlapped by an adjustable amount so that the location of a given source can be based on the centroid of the solutions from a number of windows.

The process of determining $\hat{\tau}_d$ for a single window is depicted in Figure 2 for an impulsive radiation event at the beginning of the flash discussed in section 4. Figure 2a shows a 256 sample window of the recorded waveforms for two of the receiving channels, with the vertical scale representing normalized amplitude after digital filtering was used to further attenuate noise sources outside the 20–80 MHz band. Close examination shows that the channel 1 signal (blue) is slightly advanced relative to channel 2 (red). The oscillatory nature of the waveforms is due to the bandpass filter being shock excited by a relatively short duration,

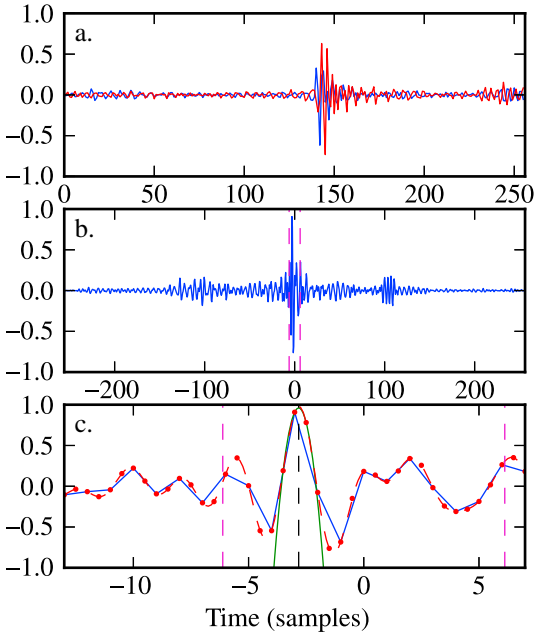

Figure 2. A temporally isolated radiation event at the beginning of the flash of section 4, illustrating the processing technique used to determine the time difference τ_d of arrival at two antennas. (a) Normalized waveforms from the two channels for a 256 (1.42 μs) sample window, after digital filtering to remove signals outside the 20–80 MHz bandwidth; (b) cross correlation of the two signals; (c) expanded view of the cross correlation around its peak, illustrating how the sampled data (blue lines) are upsampled (red dots). Three points around the peak are then parabolically fitted (green curve) to accurately determine the arrival time difference τ_d (black-dashed line), allowing τ_d to be determined to a small fraction of the sampling period. The red-dashed lines indicate the maximum physically possible τ_d for 10.2 m baselines (±6 samples about zero lag).

impulsive radiation event. An impulsive excitation causes the bandpass filter to ring at its center frequency $f_c = 50$ MHz, corresponding to ≃4 samples of the digitized waveform. For a receiver of bandwidth $B = 60$ MHz, the ringing dies out in a time Δt approximately equal to 2–4 times $(1/B)$, or about 33–66 ns (6–12 digitizer samples).

Figure 2b shows the full cross correlation of the two signals, with a peak near zero offset. The horizontal axis indicates the time lag of the correlation, which extends over ±256 samples. The vertical axis is normalized correlation coefficient with maximum limits of ±1. Figure 2c shows a zoomed-in plot of the correlation peak. The piecewise-linear blue line connects the sampled points at time intervals $T_s = 1/180$ MHz ≃ 5.6 ns. The cross correlation oscillates at the same frequency as the ringing which, because the recorded spectrum is roughly constant across the 20–80 MHz band, corresponds to the center frequency of the band (50 MHz), or ≃ 4 samples per period, as above. In addition, significant correlation dies out beyond about a six-sample interval, consistent with the $(1/B)$ estimates given above.

Although the sampling fully satisfied the Nyquist criterion (i.e., 2 or more samples per period), it is a bit too coarse for parabolic fitting to accurately estimate the peak. To rectify this, the waveform is upsampled by a factor of 2 or more, in a manner that does not alter the frequency content of the waveform (for example, by zero-padding the two $X_i(f)$ spectra used in determining the cross spectrum). The red points show the cross correlation when the individual waveforms are upsampled by a factor of 2. While it is possible to upsample the waveforms with arbitrarily fine precision to determine the cross-correlation peak, doing so would be much more computationally intensive than fitting a parabola to three upsampled points about the maximum. If the waveform is not upsampled at all, the parabolic fit would introduce error and cause the peak to be mislocated. Upsampling by a factor of 4 results in the difference between the peak determined with a parabolic fit and that obtained by excessive upsampling being much less than the timing uncertainty fundamental to the measurement (see section 3.4). The green curve in Figure 2c shows the parabolic fit to three points about the maximum. The cross correlation quickly deviates from the parabolic fit, but near the

maximum, the fit is good. The black-dashed line is the resulting time delay estimate and does not fall on a sample boundary.

The 256 sample windows are purposely overlapped so that the location of a single emission source can be based on the weighted centroid of the solutions from successive overlapping windows. Increasing the fractional overlap improves the quality and number of solutions at the expense of processing time. For the results shown in this paper, a 98% heavy overlap (all but four digitizer samples overlapping) was used for all figures. Thus, a given time-isolated event would be detected in as many as 256/4 = 64 overlapping windows.

The overlap procedure requires a method for determining if the solution from a given window corresponds to the same emission as the solution from a previous window. Two windows are considered to contain the same emission if the time between the peak value of successive windows is less than half the window length (0.71 μs). This criterion has the effect that two sources can be located in a single window, particularly in the case of continuously radiating source, but does not otherwise significantly affect the results of the calculation.

The weights for the centroid calculation are based on the closure delay, defined as

$$\tau_{123} = \tau_{12} + \tau_{23} - \tau_{13}, \tag{8}$$

where the indices indicate the antennas involved in the time difference. The closure delay is closely related to the closure phase used in astronomical interferometers. If the emission is from a distant point source, the expected closure delay is zero. The closure delay from a nonsymmetric distributed source will deviate from zero. In addition, because the time delay measurement is imperfect, the measured closure delay will vary on the same order as the time delay uncertainty (see section 3.4 below). Typical values of the closure delay are much less than the sampling period of the digitizer; however, if the wrong peak was chosen from the cross correlation due to noise effects, the closure delay greatly deviates from zero. The weighting used is such that solutions with large closure delay are excluded from the mean, while those with reasonable closure delay are weighted roughly equally.

Finally, it should be noted that the actual time resolution of the observations is substantially better than that of the 256 sample (1.42 μs) window approach described above. In particular, as can be seen from Figure 2, a given time window could contain the responses to multiple impulsive events, but only one power weighted mean location is determined for the relatively long window. More detailed observations could be obtained by shortening the window length, or by examining the raw waveform data.

A given window could also be completely filled by continuously radiating events such as stepped leaders and dartleaders to ground, or analogous breakdown during intracloud discharges, in which case the radiation centroid (again weighted by the strongest activity) will be located as a function of time in the successive overlapping windows, again with correspondingly higher time resolution. The ability to locate both continuously radiating and impulsive events is one of the major advantages of interferometric versus time-of-arrival measurements. Another advantage is that interferometric measurements can be processed to generate spatial *images* of simultaneously radiating events during each time window, rather than just a centroid location, as in radio astronomy interferometry (see section 5.3).

3.2. Noise Reduction

Continuous recording of the radiation signals, coupled with the coherent nature of the measurements, substantially increases the sensitivity and number of locatable events during a discharge. However, it also produces numerous solutions that are either contaminated by or entirely produced by noise. The noise comes from a number of different sources: thermal receiver noise, transmitters, reflections, local power transients, etc. The correlation technique is robust against all uncorrelated noise and narrowband correlated signals, but broadband correlated noise exists that can significantly degrade the solutions.

The magnitude of the noise problem becomes evident by noting the digitizing goes well into the ambient noise levels of each receiving channel, and that correlation peaks are obtained for all windows of the data record. One second's worth of data contains $1/(1.42\ \mu s) \simeq 700,000$ nonoverlapping windows, each of which gives a correlation peak. For heavily overlapped windows, the number of solutions is larger by a substantial factor. Because noise-only peaks will be randomly distributed over the ±1.42μs (±256 sample) time interval, most can be discarded on the basis of the transit time constraint between antennas, mentioned earlier. For $d = 10.2$ m baselines, physically possible correlation peaks have to be within ±34 ns (±6 samples) of zero.

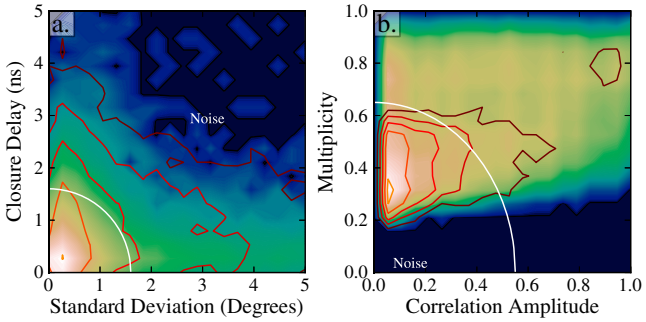

Figure 3. Contour plots of the location solutions in the metric spaces used to remove noise and noise-contaminated solutions. (a) The solutions are first filtered based on closure delay and standard deviation, with solutions having large values of either likely being in error. (b) The remaining solutions are further filtered based on normalized multiplicity and correlation amplitude, with solutions having small values of either likely being contaminated by noise. The decision boundaries used for this study are shown by the white circles. The red-black contour lines in each panel correspond to noise-only solutions outside the azimuth-elevation domain of the flash, while the filled blue-yellow-white contours correspond to flash and noise or noise-contaminated solutions inside the flash domain (see text and Appendix A).

Geometrically, exceeding the transit time constraint corresponds to the source lying outside the unit circle in the direction cosine projection plane of the measurements. This enables ≃ 98% of noise-only windows to be eliminated from consideration. However, numerous noise events still remain in the data.

The example flash of this study lasted 600 ms and its initial processing produced 197,000 solutions that passed the transit time constraint. An additional constraint consisted of requiring that at least two out of the many possible overlapping windows contributed to the solution. The result of this "phase 0" filtering is shown in Figure A1. About 168,000 sources remained, in this case consisting largely of lightning sources but leaving many noise and noise-contaminated solutions.

Further filtering of the observations using an amplitude-based threshold is unsatisfactory, as it removes important low power sources such as those associated with positive breakdown. Instead, noise and noise-contaminated solutions are best discriminated against by the use of metrics. After considerable experimentation, the following four metrics have been found to provide a basis for good quality filtering: (i) mean closure delay, (ii) standard deviation about the centroid, (iii) multiplicity of contributing windows, and (iv) normalized correlation amplitude. The first three metrics are made possible by the overlap analysis procedure, which provides a distribution of solutions weighted by the closure delay, as described in the preceding section. Multiplicity is defined as the number of windows contributing to a solution divided by the maximum number of windows which can contribute to a solution. For the window length and fractional overlap used in this study, as many as 64 windows can contribute to a solution, as stated previously. This normalized definition of multiplicity is used so that the metric is independent of the fractional overlap used during processing.

Figure 3 shows contoured data for the flash of section 4 in the above metric spaces. To aid in the filtering, the sources are partitioned into two regions according to whether they lie within or outside a trapezoidal azimuth-elevation box containing the flash. Of ≃168,000 total locations, 139,000 locations lie within the box and are a combination of actual and partially contaminated lightning sources and fully random noise correlations. About 29,000 locations lie outside the box and therefore are noise-only or badly contaminated solutions, whose characteristics are separately identified and useful in the filtering.

The noise reduction using metrics is done in two steps or phases. In phase 1, the sources are filtered in the two-dimensional space of closure delay versus standard deviation (Figure 3a). Locations having large values of either are likely to be in error and are eliminated from further consideration. To aid in determining the exclusion boundary, the two sets of partitioned sources are separately contoured, with sources inside the lightning-likely box being shown as the solid blue/green contours and noise-only sources shown as red/black contour lines. Both sets of contours peak for small closure delays and standard deviation. The contours are also circularly shaped, so a circular decision boundary (shown in white) has been used for the filtering, with sources inside the circle being retained and sources outside the circle being eliminated. The radius of the circle was determined by subjectively evaluating the results. Figure A2 shows the results of

the phase 1 metric filtering. About two thirds of the noise-only sources were eliminated, whereas 83% of the lightning-likely sources were retained.

The second phase of the noise reduction filters the locations in terms of their centroid multiplicity and correlation amplitude (Figure 3b). In this case, sources having low values of either metric are suspect and eliminated. Inversely, locations having large values of either (or both) are likely to be actual lightning sources. As before, both sets of contours have similar peaks, in this case in the excluded region of low correlation amplitude and multiplicity. But the noise-only sources (red/black contours) are significantly more restricted both in terms of multiplicity and correlation amplitude, enabling them to be discriminated against relative to the lightning-likely sources (yellow to white contours). For simplicity, because very few sources have multiplicities less than ~0.2, a circular decision boundary is again used, in this case with sources outside the white circle being retained.

Figure A3 shows the final results of the filtering. The number of noise-only sources outside the partitioning box has been drastically reduced, by 95% to less than about 600 sources, while 56% of the sources within the box have been retained. Comparing Figures A2 and A3, it is recognized that the phase 2 filtering may not be needed, particularly when having as many lightning sources as possible is important.

Overall, the metric filtering removed about half of the physically possible sources. Despite this, for the example flash of this study, $\simeq 65,000$ sources were obtained during the 600 ms duration of the flash (Figure 5). This corresponds to the flash-producing locatable VHF radiation for about 15% of its duration.

3.3. Effects of Windowing Functions and Window Length

The effect of windowing functions on the generalized cross correlation is important, but not dramatic once significant correlated noise sources are removed. Use of the W_l window increases the number of low-amplitude sources that are located and causes the locations of these sources to exhibit less random spreading, as quantified in a measurable reduction in angular uncertainty (see section 3.4 below). The improvement is most noticeable for low-amplitude sources and therefore is important in studying breakdown associated with positive leaders. The additional low-amplitude solutions account for an increase in the total number of locations after metric-based filtering, from about 57,000 with no windowing to 63,000 using W_l. Because of the increased sensitivity, there is a corresponding increase in noise-affected solutions. The additional noise sources are largely due to the lightning radiation events being contaminated by noise, which predominantly affects the low-amplitude solutions. The metric-based filtering enables the majority of the contaminated noise events to be removed.

The results presented in this paper were obtained using 256 sample (1.42 μs) windows, each upsampled by a factor of 4 before using a parabolic fit to obtain the correlation peak. The effect of shortening the window length resulted in a significant increase in the number of solutions, but a proportionally larger increase in noise-contaminated solutions, as well as a modest increase in angular uncertainty. As the window length is increased, the effect of noise on the correlation approaches the ensemble average of zero, whereas for shorter window lengths the noise is less well averaged out and has a greater effect. There is thus a tradeoff between reducing the window length to increase the number of located sources and increasing the window length to minimize noise contamination. Empirical tests indicated that a 256 sample (1.42 μs) window length produces optimal results. Shorter window lengths may be desirable for more active flashes or for faster propagating emissions, where longer window sizes would include multiple source locations.

3.4. Angular Uncertainty

The uncertainty of the time delay estimation governs the angular uncertainty of the interferometer. The variance of the time delay estimation can be found from the Cramer-Rao Lower Bound. The minimum variance of any time delay estimator with constant signal-to-noise power spectra is given by [e.g., *Carter*, 1987]

$$\sigma_\tau^2 \geq \frac{1}{2T\int_{f_1}^{f_2}(2\pi)^2 \frac{1+2\cdot \mathrm{SNR}}{\mathrm{SNR}^2} f^2 \mathrm{d}f}, \tag{9}$$

where T is the integration time, f_1 and f_2 are the lower and upper frequency bounds, and SNR is the linear signal-to-noise ratio. This can be rewritten in terms of the center frequency f_c and bandwidth B as

$$\sigma_\tau^2 \geq \frac{3}{8\pi^2}\frac{1+2\cdot \mathrm{SNR}}{\mathrm{SNR}^2}\frac{1}{BT(3f_c^2+B^2/4)}. \tag{10}$$

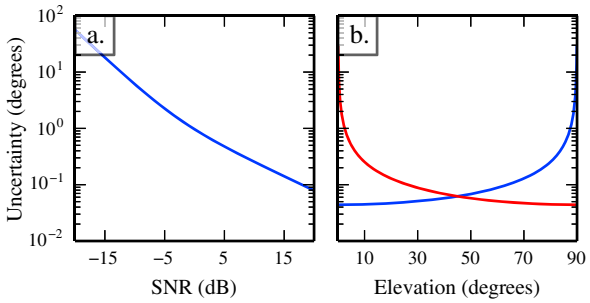

Figure 4. Effect of signal-to-noise ratio (SNR) and elevation angle on the angular uncertainty of the broadband interferometer. (a) Angular uncertainty versus SNR for an elevation angle of 45°. (b) Angular uncertainty of the elevation angle (red) and azimuthal uncertainty (blue) versus elevation angle (blue) for SNR = 3 dB.

This uncertainty is a lower bound; the actual uncertainty may be greater than this, especially in situations with low SNR [*Carter*, 1987]. An error analysis of equations (4) for determining the azimuth and elevation from the measured time delays gives

$$\sigma_{\mathrm{Az}} = \frac{c}{d}\frac{1}{\cos(\mathrm{El})}\sigma_\tau \tag{11}$$

$$\sigma_{\mathrm{El}} = \frac{c}{d}\frac{1}{\sin(\mathrm{El})}\sigma_\tau\,. \tag{12}$$

For the parameters of this study (Table 1), the RMS timing uncertainty of the interferometer is $\sigma_\tau \simeq 0.11$ ns for signals with an SNR of 10 dB. For antenna spacing $d = 10.2$ m, the angular uncertainty at 45° elevation is $\sigma_{\mathrm{Az}} = \sigma_{\mathrm{El}} \simeq 0.25°$. The effects of changing SNR and elevation angle are depicted in Figure 4.

We note that the timing uncertainty σ_τ (0.11 ns) is much smaller than the sampling period of the digitizer, $1/f_s = 5.5$ ns. The reason such a small timing uncertainty is possible is because the time delay is calculated by coherently comparing (i.e., "interfering") the signals from pairs of antennas. Such small timing uncertainty requires that the sampling rates of the digitizers are synchronized to better than the expected timing uncertainty. The timing uncertainty calculation is broadly applicable; the assumptions made to arrive at the lower bound are that the measured signal is coherent, stationary, and Gaussian, and that the noise in each channel is uncorrelated. The lower bound timing uncertainty works equally well for any method that estimates time delay and meets these criteria, including narrowband and broadband interferometry using phase fitting.

In addition to the angular uncertainty, the interferometer also has an angular resolution related to its overall aperture size. From classical diffraction theory, the angular resolution (i.e., the ability to distinguish between two adjacent sources) is approximately $\Delta\theta = \lambda/d$, where for a broadband system λ is the shortest wavelength and d is the longest baseline. For lightning interferometers, the angular resolution is relatively large because the aperture is usually a small number of wavelengths. In the present case, the aperature at 80 MHz is $d \simeq (8/3)\lambda$, for which $\Delta\theta = 3/8$ radian, or ≃20°. In terms of the correlation measurements, this corresponds to the width of the cross-correlation ringing, seen for example in Figure 2b. From the figure, it is evident that sources closer together than the width will be indistinguishable. In this case, i.e., for sources closer together than 20°, an intermediate location is determined by the algorithm.

3.5. Measured Uncertainty

The effects of the angular uncertainty relations described above can be seen in the maps of lightning flashes. From (10), it is expected that the angular uncertainty of strong sources will be less than that for weaker sources. Indeed, and not surprisingly, Figure 6c, in which the sources are colored by received amplitude/power, shows that the stronger amplitude (red or light green) sources more clearly define the breakdown channels in both the positive and negative breakdown regions than the low-amplitude (blue/dark green) sources.

The actual angular uncertainty can be estimated from the data by examining clusters of points. A cluster is broadly defined as a 25 μs window having 10 or more sources, and where at least half of the sources are contained within a 5° × 5° box between 30° and 60° elevation. Such clusters are produced, for example, at the tip of propagating negative leaders, and as localized, stationary activity prior to the onset of negative leaders. The angular uncertainty is calculated by subtracting the mean location of each cluster and computing the standard deviation about the mean for all clusters. Using this approach, the angular uncertainty is estimated to be $\sigma_{\mathrm{Az}} = 0.82°$ and $\sigma_{\mathrm{El}} = 0.63°$, based on 3262 sources in 307 localized clusters. This is a stochastic measure of the uncertainty; the width of a channel containing 95% of the sources located by the interferometer would be 4σ. The analysis assumes a localized emission source that is not moving and that all sources in the flash have the same uncertainty. However, it is clear that the sources in a given cluster will progress some distance in the 25 μs window, which will increase the estimated angular uncertainty. The uncertainty is also a function of elevation angle and received amplitude, which also is generally different from one cluster to

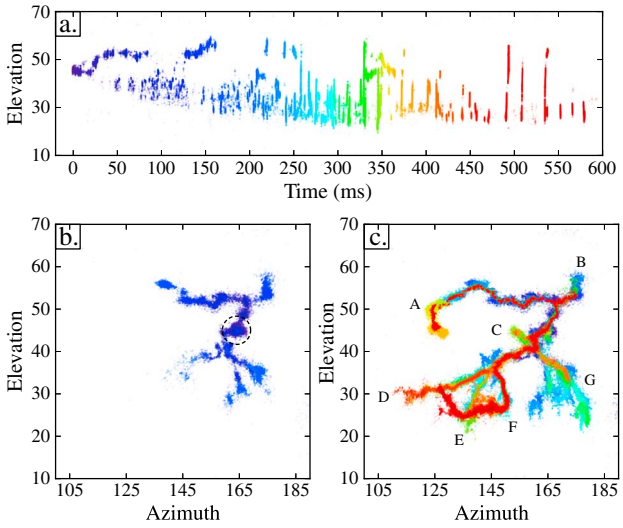

Figure 5. Interferometer observations of a bilevel intracloud flash on 22 June 2012 at 03:08:10 UTC, 8–10 km distant from the interferometer site. (a) Elevation angle versus time; (b) azimuth versus elevation of the sources during the first 200 ms of the interferometer record, (c) sources for entire flash. The interferometer record began 8 ms into the flash, and the coloring indicates time. Because the flash was well oriented with respect to the interferometer, elevation angle primarily indicates altitude. Upper level channels A and B correspond to negative leaders propagating into upper positive storm charge. Lower level channels D, E, F, and G are formed by positive breakdown propagating into midlevel negative charge. Channel C is a negative-polarity side channel that resulted from negative charge temporarily being unable to propagate up the vertical connecting channel, partway into the discharge. The dashed circle indicates the flash origin.

the next and for different sources in the same cluster. Recognizing these effects, the estimated uncertainties agree reasonably well with the lower bound values obtained from (11) and (12), which give $\sigma_{Az} = \sigma_{El} \simeq 0.25°$ at an elevation angle of 45°.

4. Observations of a Classic Bilevel Intracloud Flash

During the summers of 2011 and 2012, the interferometer was deployed at Langmuir Laboratory in central New Mexico for complementary studies with the Langmuir Lightning Mapping Array. On 22 June 2012, a storm developed near the mountaintop laboratory from which several lightning flashes were initially recorded. We discuss here a bilevel intracloud flash that occurred at 03:08:10.390 UTC, 6–8 km south and southeast of the mountaintop observatory and interferometer site. The flash time corresponds to the time of its first located LMA source. Due to the lack of pretigger capability in the 2012 measurements, the interferometer recording started 8 ms into the flash. All times for the interferometer data are in milliseconds from the beginning of its record, at 03:08:10.398. Due to the storm occurring early in the 2012 field program, electric field change measurements were not yet being made for the observations.

The flash was selected for initial study because it had all the features of a classic bilevel intracloud (IC) discharge and was well situated relative to the interferometer, developing primarily in azimuth and elevation directions rather than radially. As a result, the different branches of activity were reasonably well separated in the 2-D interferometer data.

Figures 5 and 6 show overviews of the interferometer observations for the flash. The three-dimensional LMA data are shown in Figure 7. Figures 5a and 6a shows the flash development versus time, colored according to time and by received power, respectively. The flash lasted about 600 ms, with the initial 200 ms of activity shown in Figure 5b. The dashed circle indicates where the flash initiated. Figure 6b shows the source locations in the direction cosine measurement plane, which are projected up onto a unit-diameter hemisphere to obtain the azimuth and elevation locations (equations (3)). The results show the flash approximately as it would be viewed from the interferometer location.

Typical of normal polarity IC discharges, the flash began with upward negative breakdown (the green sources at the beginning of the flash in Figure 7a) into and then developed horizontally through the storm's upper positive charge region (channels A and B of Figure 5, corresponding to the red sources in Figure 7). This was followed after a delay by slower-developing positive breakdown downward into and through

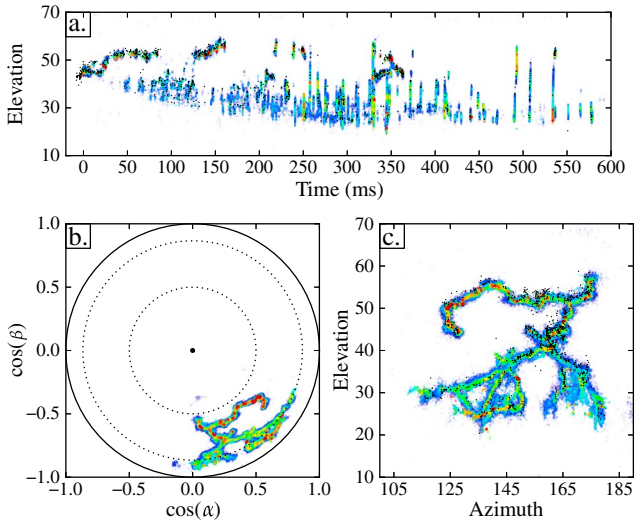

Figure 6. Same as Figure 5, except with the sources colored by peak correlation amplitude (power), and showing the sources in the direction cosine plane of the measurements (Figure 6b). LMA observations of the flash are overlaid as small black dots in Figures 6a and 6c. The direction cosine plane is equivalent to the phase plane of narrowband measurements. Physically realizable sources lie within the unit circle, corresponding to the transit time constraint at horizontal incidence. The azimuth and elevation results are obtained by projecting the direction cosine locations up onto the unit celestial hemisphere, whose equator corresponds to the unit circle and whose zenith (black dot) is directly above the interferometer [e.g., *Rhodes et al.*, 1994]. The dashed circles correspond to 30° and 60° elevation and illustrate how sources at elevation angles below about 30° are located less accurately in elevation than sources at higher elevation (Figure 4b).

midlevel negative storm charge. The latter activity established lower-elevation branches D, E, F, and G, corresponding to the blue sources in Figure 7. Whereas the negative breakdown produced only three leader channels and developed intermittently with time, the positive breakdown, once detected, developed continuously and simultaneously along multiple branches and subbranches until the final stages of the flash (e.g., Figure 5a). A prominent feature in the positive breakdown channels are a succession of fast retrograde negative leaders ("K"-events, also referred to as "recoil" leaders) back along inferred positive leader paths within the negative charge region. The K-events are seen as vertical lines in the elevation/height versus time panels in both the interferometer and LMA data (Figures 5a and 7a). For much of the flash, the K-activity served to supply additional negative charge into still or partially conducting main channels, and from there into the storm's upper positive charge. The retrograde leaders initiated along the farthest few kilometers of the previously detected activity in the positive breakdown region, and tended to cease radiating upon entering main conducting channels. As in the study by *Shao and Krehbiel* [1996], some of the K-leaders radiated along the full extent of the channel, beginning in the middle stages of the flash, but particularly in final stage, indicating that the channel conductivity was decreasingly sustained as the flash matured and neared completion.

Figure 6 shows how the LMA sources (small black dots) compare with the interferometer data, both temporally and spatially. The comparison is obtained by transforming the 3-D LMA data into the two-dimensional azimuth-elevation coordinates of the interferometer. Although the LMA data were obtained from a minimal number of stations (7), it imaged the lightning discharge in reasonable detail and the results agree exceedingly well between the two sets of observations. This is to be expected, given that both instruments measure the emissions in the lower VHF. Figure 6 also illustrates how the negative leader sources have stronger peak power values than those associated with the positive breakdown, consistent with similar findings in LMA observations [e.g., *Thomas et al.*, 2001]. The source power differences are seen more clearly in Figure 10a.

Partly by coincidence but primarily the result of being a common type of discharge, the example flash of this study was very similar to flash 163057 studied interferometrically by *Shao* [1993] and *Shao and Krehbiel* [1996] in a Florida storm on 23 August 1992. In turn, both are similar to IC flashes during TRIP 1977 at Kennedy Space Center, whose electrical charge transfer was studied in detail by *Krehbiel* [1981]. The early

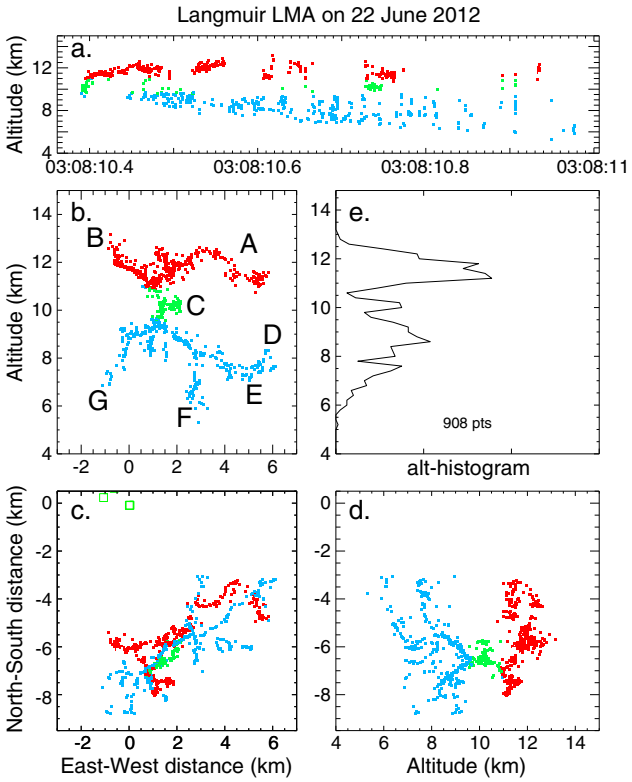

Figure 7. Three-dimensional LMA observations of the flash of Figure 5. (a) The source altitudes versus time is very similar to the elevation angle versus time plots of the interferometer maps. (c, b, and d) The sources in plan view and in E-W and N-S vertical projections. The interferometer was colocated with the upper leftmost LMA station (green square) in the plan projection and viewed the flash approximately as seen from the backside of the E-W vertical projection. The sources are colored by inferred storm charge, with the red sources being indicative of negative leaders propagating into upper positive charge, and activity associated with positive breakdown in the main negative charge region colored in blue. The green sources show the initial upward negative breakdown that connected the two charge regions. (e) A histogram of the source altitudes.

charge transfer and interferometer observations have been confirmed and expanded upon by numerous LMA observations since then, and are further expanded upon, substantially so, by the broadband interferometer observations.

4.1. Flash Development

How the flash developed is best seen from animations of the data, an example of which is available in the supporting information. Figure 8 shows a frame from the animation, 316 ms into the flash. By this time, the flash was relatively well developed in both the negative and positive breakdown regions. The light blue-colored sources in the left-hand panel show that simultaneous K-activity was occurring back along the far end of the F and G channels, with the gray background indicating the integrated VHF intensity and channel structure up to the frame time. The animation has simulated frame rates of 5,000 and 62,500 frames per second, with the higher frame rate used to show the motion of rapidly propagating events. The results are analogous to high-speed video observations of developing lightning channels at optical wavelengths [e.g., *Warner et al.*, 2013] but reveal the activity inside the storm as well as outside. Detailed analyses of the observations of this and other flashes is the subject of ongoing study; in the following, we describe selected results from the animation and LMA observations, in addition to the overall features mentioned in the preceding section.

4.1.1. Initial Activity

During the first 10 ms of the flash, the LMA data show that negative breakdown developed upward from the flash start point at 9.6 km altitude, toward and into the upper positive charge region. The leader progressed 1 km vertically to 10.6–10.7 km altitude in the first 8 ms of the flash, corresponding to a speed of 1.2×10^5 m s^{-1}. This speed is typical of the initial leaders of IC flashes [*Behnke et al.*, 2005].

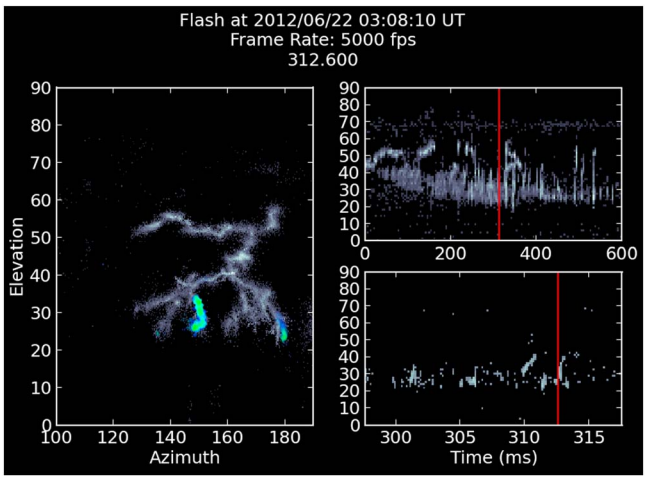

Figure 8. Sample frame from an animation of the interferometer observations, 316 ms into the interferometer record. The full animation is available in the supporting information. The left-hand panel shows the flash in the same azimuth-elevation view as Figure 5. The light gray background channels show the accumulated prior activity and the colored points indicate the radiation intensity (power) of the current activity, with approximately 10 frames of persistence. The right-hand panels show elevation angle versus time, both for the entire flash and for an expanded time period before and after the current frame. The red lines indicate the time of the current frame. The simulated frame rate (top center) alternates between slow (200 μs/frame) and fast (16 μs/frame) rates during the animation to allow the development of faster moving processes to be seen.

The start of the interferometer record corresponds to the beginning of horizontal development within the upper positive storm charge. During the first 20 ms of the record, the radiation remained localized at about 45° elevation and 165° azimuth. From the LMA data, the radiation during this time was produced by the beginning segments of two horizontal branches that developed over ~1 km distances toward and away the interferometer, causing the sources to have a stationary appearance in the 2-D data. At 23 ms, the closer negative leader turned upward again, establishing the initial part of channel A. Subsequently, channel A developed horizontally, propagating ~4 km northeastward in 64 ms at an estimated average speed of 6×10^4 m s^{-1}, a factor of 2 slower than the initial upward leader speed. Similar speed decreases were observed in LMA observations of IC flashes by *Behnke et al.* [2005].

Also, as in LMA observations of IC flashes, the interferometer data show a delayed onset of detected VHF radiation from downward positive breakdown. The first indicated VHF activity associated with the positive breakdown occurred 23 ms into the interferometer record (31 ms into the flash). The first located LMA source associated with the positive breakdown occurred 24 ms later, 55 ms into the flash. The delay is due in part at least to the weaker positive radiation being masked by stronger radiation from the developing negative breakdown, as found, for example, by *Edens et al.* [2012]. But it may also be due to the positive breakdown being inherently weak initially, or not immediately occurring. After being detected, the positive activity increased slowly and somewhat randomly with time, revealing a gradually lengthening breakdown path.

Eighty-five milliseconds into the animation, the negative leader temporarily stopped developing. The cessation is readily seen in the height-time panels of both the interferometer and LMA data (Figures 5 and 7), and gave rise to a relatively RF quiet interval during which the positive activity was more readily detected. Cessations and intermittent rejuvenations of the negative breakdown are a common feature of LMA observations of IC discharges and imply that the positive breakdown supplies insufficient charge to keep the negative breakdown active. (In this sense intracloud discharges are similar to multistroke negative cloud-to-ground discharges, whose positive breakdown is the same as that of normal polarity IC flashes and favors multiple discrete strokes over continuing currents.) By the time of the initial cessation, the positive activity extended the vertical trunk downward and a short distance rightward into the beginning part of channel G. The RF-quiet period lasted 41 ms, up until 126 ms, during which time the positive activity advanced further downward and outward, simultaneously along three fronts—the initial parts of the two main G branches and the start of the left-hand branch D.

At 125.800 ms into the animation, renewed negative breakdown started at the top of the upward trunk in the upper part of the storm, and began establishing negative channel B. Five milliseconds later, at 131.072 ms, negative breakdown began halfway along channel A that reactivated the remainder of that channel and extended it further northeast. The rejuvenation and extension appeared to be initiated by impulsive breakdown 880 μs earlier, at 130.192 ms, at the opposite, positive breakdown end of the flash. The breakdown in question initiated at the far tip of the low-elevation subbranch of channel G and appeared to propagate backup the branch as a retrograde negative leader and possibly a short distance downward beyond the tip as positive breakdown. Altogether, it is an early instance of a K-type retrograde event rejuvenating and extending the upper level negative leaders. The ensuing extension of channel A lasted 32 ms, ending 163.000 ms into the record and beginning another RF-quiet interval where the positive activity became more detectable.

4.1.2. Positive Breakdown

Development of positive breakdown in the storm's midlevel negative charge region was more complex than that of negative breakdown in the upper positive charge region. Whereas the negative breakdown radiated primarily from its leading edge and advanced intermittently with time between relatively long quiet intervals, the positive breakdown was more continuous and did not have quiet periods. Rather, it produced continual "flickering" VHF activity quasi-simultaneously along a number of developing subbranches. The flickering continued over the first 400 ms or so of the flash, with an increasing number of stronger K-events superimposed on it, before gradually dying out in the final stages.

For the first 230 ms or so of the animation, the VHF activity in the positive breakdown region consisted primarily of flickering events that gradually revealed multiple branches and subbranches of the positive channels. Initially, the flickering tended to be randomly distributed along the developing channels but it increasingly occurred at or ahead of the advancing tips of the detected channels (e.g., at 177.400, 205.616, 214.016, and 237.208 ms, and numerous other frames). A few events appeared to propagate in a forward direction as positive breakdown (e.g., at 109.400 and 130.960 ms). Superimposed upon this activity was a steadily increasing number of short-length negative retrograde events that further illuminated the developing channels.

At 239.016 ms, negative breakdown reinitiated again along channel A, this time back at the beginning of its horizontal channel. The breakdown rejuvenated the extension of channel A yet a second time, in so doing producing VHF radiation along the full length of A. That the leader produced radiation indicates that the channel had become nonconductive sometime during the 76 ms interval since it last appeared to be active. The negative leader that rejuvenated the channel appeared to initiate on its own, with no precursor event detected in the positive breakdown region. Presuming that charge was continually transported into the upper part of the storm during the early stages of the flash, as found in the Florida studies, such charge transfer would have been occurring throughout the 76 ms quiet interval after channel A had died out. The rejuvenating breakdown could have been initiated simply by the increasing accumulation of negative charge at the base of A, rather than by a K-event in the positive breakdown region.

More pertinent to the discussion of positive breakdown, within about a millisecond following completion of the upper level rejuvenation and extension, three retrograde negative K-events occurred in rapid succession along low-elevation channels at the opposite end of the discharge. The activity began at 240.608 ms in the animation and was more energetic VHF-wise than seen prior to this time. Significantly, the events occurred in branches progressively displaced from right to left within the storm, being initially along two low-elevation subbranches of channel G and finally along the lower extent of channel F. The activity appears to have been triggered by the A-extension, possibly from a propagating potential wave initiated by effects of the channel extension. A similar apparently triggered event occurred as the extension neared completion, at 239.512 ms. In this case a burst of radiation sources suddenly appeared within a 16 μs time interval a substantial distance away from the low-level channel, where no previous activity had been detected.

Before proceeding, we note that the leftmost postextension K-event in the G channel discussed above, at 240.808 ms, had the shape of an inverted "V." This resulted from the breakdown initially propagating as a retrograde leader up the subbranch on the right and, upon reaching the bifurcation point with an adjacent subchannel, sharply reversing directions and propagating in a forward, "prograde" direction back down the adjacent channel on the left. Such V-shaped events are a common feature of high-speed optical observations of positive leaders [e.g., *Saba et al.*, 2008; *Warner*, 2011]. It has also been observed at VHF by

Edens et al. [2012] in connection with LMA observations of rocket-triggered lightning. Rather than switching from negative to positive breakdown, the leader continued to be of negative polarity and therefore would have transferred negative charge from the right to the left subbranch.

4.1.3. Strong Positive Bursts

The above activity was followed by continued flickering and channel development along the low-elevation channels, accompanied by further extension of the upper level A channel. Then, beginning at 250.400 ms, two exceptionally bright (red-colored) VHF events occurred in quick succession off the far end of the rightmost G branch, 80 μs apart in time. Each appeared to be associated with positive breakdown away from the developing channel. Another pair of bursts occurred about 1 ms later, beginning at 251.488 ms in a nearby subbranch, that appeared to initiate positive breakdown in two different directions away from their starting point. We call these events "strong positive bursts." The cause of the two pairs of events is not clear, but their occurrence is indicative of some sort of strong potential disturbance.

Other positive bursts occurred at 328.840, 345.216, 348.416, 410.680, and 533.584 ms in the animation. The first two bursts occurred 17 ms apart in time in adjacent subbranches at the far end of the low-level channel E. In both instances, retrograde negative breakdown started at the bifurcation point of the two subbranches, well back from their tips. The breakdown propagated as a retrograde negative leader back up the E channel toward and into channel D. For the first event, the positive burst occurred at the far end of the left-hand branch, within a few tens of μs of the leader appearing to reach the junction point with D. A similar sequence of events occurred for the second burst, except that the burst followed a sudden increase in the VHF radiation by the leader as it neared the D channel, presumed to be indicative of actually connecting with D. The positive burst occurred at the far end of the rightmost subbranch, two frames (32 μs) after the leader intensification. In both cases, the bursts appear to have occurred as a result of channel D having a significantly different electric potential than that of the retrograde leader, and that this caused a potential wave to travel in a forward direction down the respective subbranches, producing the positive burst at their far end.

The third positive burst, at 348.416 ms, occurred off the end of the leftmost D channel, again in the lower part of the storm. It was similar to the above E-bursts in that it appeared to be initiated by retrograde negative breakdown reaching a junction point on the main D channel. Like the second of the two E events, its retrograde leader brightened substantially upon nearing the apparent branch point. The burst occurred 32–48 μs after the brightening, beyond the starting point of the retrograde leader. The event differed from the E-channel events in that the retrograde breakdown (at 348.272 and 348.304 ms) was immediately accompanied by oppositely directed, weaker breakdown laterally away from the channel tip. In addition, three distinct bright sources occurred well beyond the leader start point and burst location as the leader immediately prior to the leader intensification.

Each of the three burst events discussed above were part of a sequence of energetic K-events that originated in the lower left side of the storm. In each case the leader went on to propagate into the upper storm or midstorm level, along the full extent of the A, B, or C upper negative channels. The final two bursts, at 410.680 and 533.584 ms, also originated in the lower left part of the storm, at the far end of channel F. Without going into the details, it can be seen from the animation that the event at 410 ms was basically the same as the events at 325 and 348 ms, except that the positive burst occurred back at the tip of a slightly different, adjacent subbranch rather than the branch of the retrograde inception. Upon arriving in the trunk region, a weaker positive burst was initiated along yet another slightly different subbranch back at far start region. Again, the weaker burst was delayed by some tens of microseconds from the leader reaching the trunk base, indicating that it also resulted from a forward potential wave caused by attachment to a conducting channel.

We note that delayed VHF bursts back at the starting point of K-events were also observed by *Shao et al.* [1995, Figures 22 through 24]. The K-events occurred in the late stages of a negative cloud-to-ground (-CG) flash, but the positive breakdown processes and K-activity for −CG flashes are essentially the same as for normal polarity IC flashes. The bursts occurred at a high elevation angle and relatively close to the interferometer, so that the propagation direction of the bursts was readily detected. They were found to correspond to fast positive breakdown in the opposite direction away from the starting point of the negative K-leader. Their VHF radiation was brief and also exceptionally strong, even at the upper VHF frequency of the measurements (274 MHz; events "b" of their Figures 22 and 23). The bursts occurred immediately adjacent to the K-leader inception point, rather than at a distance as in the present observations, but are otherwise similar to the present results.

4.1.4. Horizontal Charge Transfer Events

At 266.584 ms, retrograde negative breakdown initiated partway down the beginning part of the F branch on the left-hand side of the flash. The breakdown propagated a short distance into and back up along the main D channel to its bifurcation point with channel G, whose branches connected into the right-hand side of the storm. The K-leader arrived at the bifurcation point 192 μs after being initiated, at 266.776 ms in the animation. From there, it split in two directions, with one branch continuing upward along the trunk into the flash initiation region, and the other propagating in a forward direction down the leftmost G channel on the lower right side of the storm. As in the case of the inverted "V" event discussed above, the downward G breakdown continued to be of negative polarity and therefore transported negative charge from the left-hand side of the storm to the right-hand side, all within the storm's main negative charge region. Similar left-to-right K discharges occurred at 295, 326, 401–403, and 410 ms in the interferometer observations, along with an earlier, somewhat weaker event at 229 ms.

The occurrence of the horizontal cross-discharging is a new finding of VHF observations for otherwise vertical IC flashes. It indicates the development of a lateral charge imbalance in the storm produced by the discharge itself. In particular, the imbalance appears to result from excess positive charge being induced in the right-hand side of the storm's negative charge region early in the flash, where the G channels initially produced most of the discharging, and by the excess charge subsequently being stranded there by channel cutoff processes. The D→G breakdown can thus be considered as a charge redistribution event that reduced the imbalance. The observations are consistent with charge transfer results for a similar IC flash in a Florida storm by *Krehbiel* [1981] (Flash 49), where dominant vertical charge transfer later became horizontal within the negative charge region.

Other instances of negative breakdown propagating in the forward direction along positive channels are seen in the interferometer observations, although less well resolved than the above large-scale activity. In these cases, the discharges have a characteristic, sharply pointed V or forked appearance, discussed above in connection with the K-activity at 241 ms. Other examples of this type of activity are listed in Table 2. The events can be considered as charge redistribution or potential equalization activity on a more local scale.

4.1.5. K Activity

As indicated earlier, negative polarity K-events were a prominent and characteristic feature the activity in the positive breakdown region. The activity took the form of a succession of retrograde negative leaders back along the inferred paths of the positive breakdown, and were undoubtedly a controlling factor in the flash development. The K-leaders connected into and rejuvenated previously conducting main channels, thereby continuing to supply negative charge into the upper positive storm levels.

Table 2 lists the times, durations, and channel lengths of 33 negative K-leaders whose VHF radiation lasted longer than a nominal value of 200 μs. The channel lengths are estimated 3-D values obtained by expanding the 2-D interferometer observations to quasi 3-D results utilizing the LMA observations (section 4.3). The estimated lengths range from about 2 km to 17 km, with the lengths of five events exceeding 10 km. As can be seen from the animation, many more K-events occurred that were of shorter duration, including ones whose propagation was not resolved by the observations but can be inferred from the number and strength of their radiation sources. Many of the K-leaders were physically and temporally short because they contacted a conducting main channel, whereupon the radiation weakened or ceased.

Figure 9 shows observations of the extensive K-event that occurred between 328 and 330 ms (labeled K-2 in Table 2), whose initiation was discussed in the previous section on positive bursts. In particular, the event began with retrograde negative breakdown being initiated at the bifurcation point of two low-elevation subbranches of channel E, and produced a strong positive burst at and beyond the far end of the left subbranch (Figure 9b). The burst is seen in the animation at 328.840 ms and appeared to occur a short time after the leader reached the main D channel. The sources are also seen in Figure 9c as the high-amplitude sources seen just beyond the region of leader inception. Preceding the leader by ≃600 μs were two impulsive LMA events (shown in grey), whose locations coincided perfectly with the initiation point of the K-leader. Close to the same time, the interferometer located a cluster of low-intensity sources slightly further down the E channel, at the location of the positive burst. The interferometer sources are obscured in the figure by the LMA symbols but can be seen in the animation. Figure 9d shows the estimated 3-D length and propagation velocity of the leader with time. The results illustrate what is also seen in the animation, namely that the leader propagated smoothly through the junction with D and along the full length of the flash to the

Table 2. Summary of K-Leaders Longer Than 200 μs Duration, and Other Activity Discussed in Section 4.1[a]

Name	Time (ms)	Channels	Duration (μs)	Length (km)	Velocity (m/μs)
	131.1	A	336	–	–
	202.4	D	512	–	–
	231.9	D	224	–	–
	229.0[b]	D-G	–	–	–
	239.0	A	919	6.50	7.06
	240.8[b]	G	–	–	–
	250.4[a]	G	–	–	–
	251.4[a]	G	–	–	–
	257.2	D-B	911	7.04	7.73
	261.9	G	342	4.54	13.24
	266.6[b]	F-G	737	5.61	7.60
	268.1	D	346	2.06	5.96
	275.2	F	506	4.64	9.16
	291.7	G	778	3.51	4.51
	293.4	G	478	4.05	8.46
	295.0[b]	D-G	1295	11.24	8.68
	309.9	D	849	3.46	4.07
K-1	325.3[b]	D-G	1071	8.46	7.89
K-2	328.5[a]	E-A	1401	16.71	11.92
K-3	330.2	E	176	–	–
K-4	330.7	F	160	–	–
K-5	344.7[a]	F-C	670	6.16	9.18
K-6	345.7[a]	E	265	4.76	17.89
K-7	347.0	F	206	3.67	17.76
K-8	348.3	D	335	3.82	11.41
	371.6	D	670	5.81	8.66
	383.4	D	603	5.86	9.72
	400.8[b]	D-E	688	6.05	8.78
	403.2[b]	G	462	1.56	3.37
	410.3[b c]	F	608	–	–
	412.4	D	256	–	–
	439.9	F	513	4.51	8.80
	448.4	D	412	4.07	9.85
	454.8[b]	D	418	2.85	6.80
	489.6[b]	F	969	7.00	7.21
	492.2	A	897	11.97	13.33
	506.9	F-C	1550	12.01	7.75
	533.5[a]	F-C	1252	11.94	9.53
	577.0	F	1216	–	–

[a]Channels are labeled in Figure 5. Length and average velocity are reported for leaders whose quasi 3-D channels were well fitted.
[b]Positive Bursts.
[c]Horizontal Charge Transfer Events.

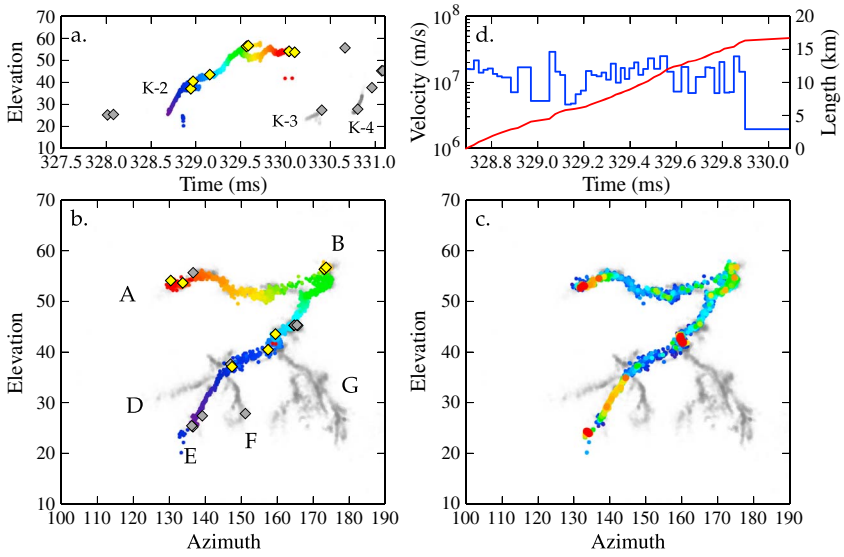

Figure 9. The extensive K-event (K-2) at 328 ms, showing the sources colored by (a and b) time and (c) radiation intensity. The intensity graph shows the occurrence of the strong positive burst beyond the starting point of the upward K-leader at the far end of channel E, and of two other strong bursts at the middle and far upper end of the negative leader. Seven LMA sources were located during the event (yellow diamonds) that are in excellent agreement with the interferometer observations, both temporally and spatially. (d) The estimated length and propagation velocity of the K-leader versus time, obtained from the three-dimensional reconstruction of the flash discussed in sections 4.3 and 4.4 and shown in Figure 11. The gray LMA sources and interferometer channels show activity associated with events K-3 and K-4, and precursor activity prior to K-2 (see text).

far end of the upper level A channel, at an average speed of about 1×10^7 m/s. As will be seen later, the speed decrease at the beginning of the leader (from 2 to 3 $\times 10^7$ m/s down to $\simeq 1 \times 10^7$ m/s) is a statistically significant result when averaged over the different K-events of Table 2.

As mentioned previously, the above K-event was the second in a series (or "swarm") of eight energetic K-events between 325 and 350 ms and that originated in the lower left part of the storm. The K-events are identified as K-1 through K-8 in Table 2. The first event, K-1, was confined to the lower level channels and transferred negative charge from the leftmost extremity of the D channel horizontally across to the G channels on the right side of the storm. This happened in the same manner as the horizontal charge transfer K-event at 266 ms discussed earlier—namely as retrograde negative breakdown up to the bifurcation point of channels D and G and then in a forward or prograde direction down the G channels. Having presumably neutralized a lateral charge imbalance between the two regions of lightning activity, the energetic K-2 event developed directly through the D-G bifurcation point, ignoring channel G, along the upward connecting channel and into the upper positive charge region, where it traveled along the full extent of both the B and A channels.

Within 130 μs of K-2 dying out at the far end of channel A, new K breakdown (K-3) commenced at the opposite end of the flash, this time at the far tip of the right-hand subbranch of E, adjacent to the subbranch involved at the beginning of K-2. K-3, seen starting at 330.216 ms in the animation and also as the minimally extensive interferometer sources in Figure 9a, propagated up to the bifurcation point of the two subbranches, where its arrival was heralded by an impulsive LMA event. Shortly afterward, at 330.376 ms, a strong positive burst occurred back at the inception point, presumably as a result of the K-leader having connected into the still conducting channel of the preceding strong K-event. This was followed in the next 16 μs frame by a strong VHF pulse at the bifurcation point, after which the VHF activity ceased. The entire event lasted 176 μs and is an excellent example of a K-event whose VHF radiation was "abbreviated," apparently by connecting into a conducting channel. A full understanding of such events requires fast electric field change observations and is the subject of continued study.

Immediately following K-3 (and possibly even as a result of it), the next major K-event, K-4, began at 330.728 ms at the far end of channel F. In this case, and as seen in Figure 9a, an impulsive LMA source was detected at the very beginning of the K-leader, well colocated with the leader initiation point. As a result

of occurring within 0.6 ms of K-2, and while the main channels were presumably at least partially conducting, VHF radiation from K-4 leader was sparsely detected along the main D, apparently indicating that D was at least still partially conducting. Sufficient radiation was produced to indicate that the leader traveled to the far upper extent of channel B, but apparently not into channel A. Rather, at the same time that activity ceased in channel B, at 331.288 ms, lateral breakdown activity began lower down along the middle right side of the upward trunk, indicating the forging of new negative channels there. The lateral breakdown continued for about 1.1 ms until, at 332.408 ms, breakdown activity also started a bit further down the main trunk that formed the negative-polarity side channel C. Development of the C channel was relatively slow, requiring 10 ms to progress on the order of 1 km distance, corresponding to a speed of $\simeq 10^5$ m/s—typical of negative breakdown into virgin air.

Formation of channel C ended at about 342.608 ms. At 343.208 ms, 0.8 ms later, weak breakdown began at the tip of the complex branch structure at the far end of the E channel that initiated brighter breakdown in a forward, positive-polarity direction into apparently virgin air, out to well beyond the tip. The positive breakdown occurred in parts of two frames, at 344.208 and 344.408 ms, before dying out. It effectively extended the detected F channel on the order of a couple hundred meters, finishing at about 344.408 ms. Subsequently, at 344.752 ms, a negative K-leader, K-5, initiated back at the starting point of the positive breakdown that propagated as a retrograde negative leader back up the E channel. The leader arrived at the junction with channel F at 345.168 ms, producing strong VHF radiation apparently just before arriving at the junction and continuing on through it. At 345.200 and 345.216 ms, 32 μs after the strong radiation near the F junction, a clear, strong positive burst and forward leader developed into virgin air in a slightly different divergent direction than the earlier positive leader at 344.2 ms. This is the second of three positive bursts discussed in the strong positive burst section. The path of this breakdown resembled that of electric field lines converging onto the tip of an elongated conductor. By the time of the second positive channel extension, the K-leader was propagating in the main D channel, where it produced two weak, side extensions laterally away from D, seen at 345.200 and 355.216 ms in the animation. Upon arriving in the vicinity of channel C, instead of continuing on up the vertical connecting channel, it turned into C and propagated laterally out along the C's full extent, ending at about 345.552 ms.

A strawman interpretation of the above activity, namely the formation of channel C and the diversion of K-5 into C, resulted from the upward channel above the flash initiation point becoming cut off by negative resistance effects and consequently "filling up" with negative charge still trying to reach the positive charge region, thereby forcing K-4 to produce channel C and K-5 to be diverted into C. This interpretation is probably questionable, as K-5 was immediately followed 1.0 ms later, at 345.776 ms, by K-6, that did not radiate along any of the upward channel or along the full length of A, but may have been the cause of a brief burst of VHF radiation 380 μs later, at 346.160 ms, beyond the far end of channel A. If the cause, the channels were likely fully conducting, In which case some other explanation is required for the channel C activity.

The above examples illustrate the kind of detailed information that is contained in the interferometer and LMA observations. Of particular note is the excellent agreement and complementary nature of the interferometer and LMA data.

4.2. Waveform Separation

Because the flash orientation was such that the positive and negative breakdown regions were well spaced, it is relatively easy to identify and separate out VHF waveforms for the two regions. Figure 10 shows the results of doing this for the first 200 ms of the flash. Recall that during this time interval, there were two distinct episodes of upper level negative channel development, each followed by relatively long (tens of millisecond) periods of no apparent growth or VHF activity. The overall state of the flash development after 200 ms is seen in Figure 5b.

The upper level sources enclosed by the dotted red box in Figure 10a correspond to negative polarity breakdown within the storm's upper positive charge—almost entirely through virgin air. The dashed blue box encloses sources associated with positive breakdown in the midlevel negative charge region. The coloring of the points indicates the peak amplitude of each source.

Figures 10b and 10c show raw time series data for the upper and lower sources, respectively. The coloring indicates the density of events. For purposes of comparison, the two sets of waveforms are plotted on the same vertical scale (corresponding to ±20 mV at the digitizer input, equivalent to −63 dBm received

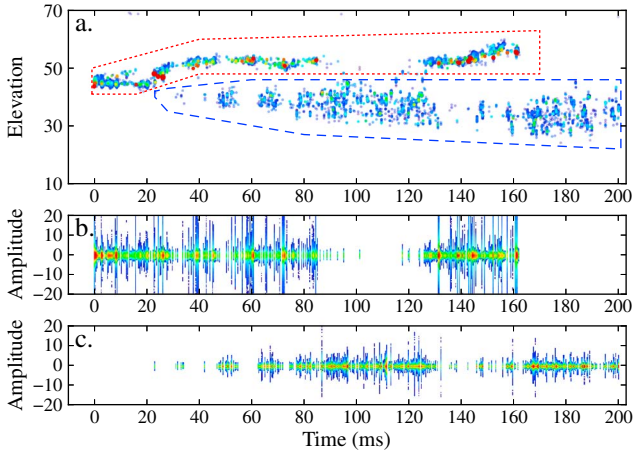

Figure 10. Partitioning of the raw time series waveforms into emissions associated with the (b) upper level negative breakdown (red-dotted box in Figure 10a) and (c) lower level positive breakdown (dashed blue box in Figure 10a), plotted with the same amplitude scales to illustrate the differences in emission intensity for the two types of activity. Color indicates (a) radiation intensity and the density of emission events in Figure 10b. The time between large-amplitude pulses in the negative waveforms may indicate stepping intervals of the leader.

power out of the flat plate sensing antenna). With this scaling, the waveforms from large-amplitude negative breakdown events frequently exceed the plot limits.

It is evident that the emission from negative breakdown events has higher peak amplitudes than the emission associated with positive breakdown. The larger negative leader emissions are typically 10 dB stronger (a factor of $\sqrt{10} \simeq 3$ times larger voltage-wise) than those of the positive breakdown. Occasionally, the voltage waveform from negative breakdown region is 20–30 dB stronger (10–30 times larger voltage-wise) than that from the positive breakdown region. The relative weakness of the emissions in the positive breakdown region occurs not only to the flickering emissions but also to the retrograde negative breakdown events in the region. The same results are seen in the LMA data for IC flashes (Figure 11e) [*Thomas et al.*, 2001]. A detailed analysis of the amplitude distributions of different types of emissions will be provided in a companion paper (M. Akita et al., submitted manuscript, 2013).

There are two time period regimes seen in the negative breakdown which may be related to negative leader stepping. First are short-duration, high-amplitude pulses that are separated by 600 μs on average, and a slower cyclic build up in intensity over the course of 5–10 ms which then reverts to a lower activity level. Given a propagation speed of $\simeq 10^5$ m/s, the short-duration pulses correspond to spatial scales of $\simeq$ 60 m, and the slower build up corresponds to $\simeq$ 100–500 m spatial scales.

The emission from the positive breakdown region is lower in amplitude but is still impulsive. This is clearly seen in the animation; in part it is caused by inclusion of the largest, brightest flickers, which are produced by short bursts of retrograde negative breakdown. However, if these bright clusters are eliminated, the residual emission is lower in amplitude but the remaining events continue to be intermittent and impulsive in nature.

Both the negative and positive breakdown regions experienced periods of enhanced and diminished activity. When the negative breakdown region was very active, the positive breakdown region shows diminished activity and vice versa. This is at least partially because the processing approach located only one emission source in each 256 sample (1.42 μs) window. If both the negative and positive breakdown regions are active in a given window, the emission from the negative breakdown region will usually overwhelm the positive breakdown activity. This causes ongoing negative breakdown to "mask" any weaker positive activity. However, even when the negative breakdown was very active, not all windows contained the activity. It would thus be expected that occasional sources associated with positive breakdown would be detected, in particular during the early stages of a flash. The fact that they are not seen in the early stages indicates that the breakdown is either too weak to produce detectable VHF radiation or that it is not yet occurring.

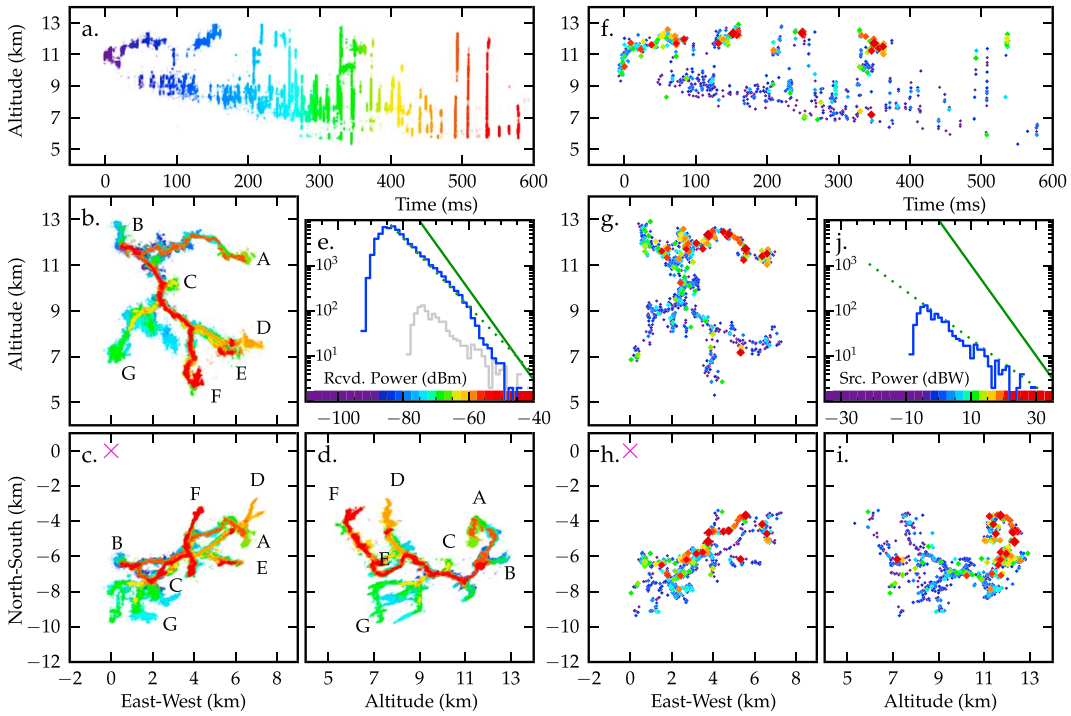

Figure 11. Quasi 3-D construction of the (left) interferometer observations compared with (right) LMA observations, illustrating how the quasi 3-D conversion works well to reproduce the LMA structure and adds substantial detail to the structure. The histograms show the distribution of measured power values P from the two systems and illustrate the sensitivity difference in the data for this particular flash (section 4.5). The solid green lines correspond to a P^{-1} distribution and the dotted green lines correspond to −0.75 and −0.53 power laws, respectively.

4.3. Quasi Three-Dimensional Conversion

In addition to projecting the LMA data onto the azimuth versus elevation framework of the interferometer observations, the inverse can be done, namely using the LMA data to infer the radial distance of individual interferometer sources. In this way one is able to construct quasi 3-D maps of the interferometer data. The conversion is best done using spatial correlations alone and not considering their relative timing. The structure of the lightning channels is better determined in the complete LMA data for a flash rather than from its temporal components.

The 3-D conversion is an iterative process that proceeds in the following manner. First, the LMA data are converted into azimuth, elevation, and range from the interferometer. Second, a crude first approximation of the 3-D projection is made for the range of each interferometer source by averaging the range values to the LMA sources that have similar azimuth and elevation values. The first conversion tends to have strong radial artifacts because there are often multiple channels in the direction of a given interferometer source. Radial smearing is also produced by asymmetric spreading in the range of the LMA sources even for single channels. The radial artifacts are removed with an iterative process that uses weighting to determine which LMA sources determine the range values. The weighting factor is the distance of the LMA sources to the iterated 3-D interferometer locations shortly before and after the source of interest. LMA sources closest to the previous and subsequent converted interferometer locations are given the most weight. In this way, a propagating event that appears to intersect with another channel in 2-D will continue on the same 3-D channel. After each iteration step, the converted 3-D interferometer locations shift, causing the weights to change. Although there is no guarantee that such an iteration will converge, in practice, it converges quickly if the interferometer data are in good agreement with the LMA locations, as in this flash.

Additionally and optionally, a piecewise-linear fit can be made to the LMA sources to more completely define each channel. This allows gaps in the LMA sources to be filled in for a given channel, which both better defines and extends the channel. The piecewise-linear fits to the LMA sources are combined with the actual LMA source locations such that both have roughly equal weight in determining the range of a given interferometer location. Overall, the weighting procedures work well to keep a moving emission on

the correct channel when the emission passes an apparent intersection in the 2-D projection. However, if the emission begins near an intersection (such as for the K-event starting at 577 ms in the animation), the algorithm can guess the wrong channel for the beginning of the emission, in which case it needs to be manually corrected. The quasi 3-D projection works best when the flash is oriented face on to the interferometer, which reduces the number of apparent intersections. Channels that are oriented radially will tend to have distorted quasi 3-D projections.

Figures 11a–11d shows the quasi 3-D interferometer images of the flash in the same format as for the LMA data. In particular, the panels show altitude versus time as well as vertical and plan projections of the inferred source locations. The channels identified in the 2-D observations of Figure 5 are correspondingly labeled. The quasi 3-D projections obviously rely on the availability of LMA data, but the LMA data do not need to be fully complete, as piecewise-linear fitting helps with the reconstruction. By examining where each added piecewise-linear fit falls in the interferometer projection, one can be reasonably certain that the added channels are placed in the correct 3-D location. Partial manual reconstruction was required to obtain good quasi 3-D projection results for channel G.

The results of the quasi 3-D conversion for this flash are very good. Ambiguities in elevation between vertical and radial development normally associated with 2-D interferometer maps are completely removed. As will be shown, the length and velocity of features of the flash not well mapped by the LMA, such as K-leaders, can be measured in the quasi 3-D constructions with a reasonable amount of confidence.

4.4. Leader Velocities of K-Events

The quasi 3-D projection results make it possible to examine the 3-D development of K-leaders in detail. In particular, by combining the high time resolution interferometer data with the 3-D structure provided by the LMA, the three-dimensional development of the leaders can be determined as a function of time and distance along their trajectory. This is accomplished by constructing piecewise-linear sets of least squares fits to the quasi 3-D interferometer results. Such fits and velocity calculations were made for all isolated retrograde leaders or leader segments over 200 μs in duration, comprising 28 events in total. Table 2 summarizes the velocity and length calculations for each event.

An example fit is shown in Figure 12 for the extensive K-2 leader discussed in the flash development section (Figure 9). It was one of the longest duration K-events of the flash, lasting 1400 μs and propagating over an estimated 16.7 km length of preexisting channel. The LMA located seven impulsive events during the leader, while the interferometer obtained 1924 location results. The large number of locations is due to the interferometer being able to follow the continuous radiation from the leader. For continually radiating events, the overlapping analysis procedure is such that it usually provides two sources per nonoverlapping 1.42 μs time intervals, and that is the case for the K-leaders. The time resolution of the processing for continuing activity is thus 0.71 μs, corresponding to 9 m spatial resolution (16.7 km/1924 locations) for event K-2. The velocity and length versus time for K-2 is shown in Figure 9c and averaged 1.2×10^7 m/s.

Figure 13 shows the mean velocity versus time for each of the K-leaders of Table 2, as a function of time over the first millisecond. Because most of the K-leaders in the flash were less than 1 ms in duration, also shown in the figure is the number of leaders contributing to the average. On average, the leaders increased their velocity over the first 200 μs followed by a slowly declining velocity. Overall, the velocities ranged from about $\simeq 0.4 \times 10^7$ to $\simeq 2 \times 10^7$ m/s (Table 2). The results agree well with 2-D speed estimates of K-events and dartleaders from the interferometer studies by *Rhodes et al.* [1994], *Shao et al.* [1995], *Mazur et al.* [1995], and *Shao and Krehbiel* [1996] and 3-D estimates by *Bondiou et al.* [1990] and *Akita et al.* [2010]. They are also in good agreement with the range of dartleader velocities obtained from similar quasi 3-D interferometer measurements by *Qiu et al.* [2012]. In the latter studies, the quasi 3-D results were obtained by combining 2-D broadband interferometer observations with three-dimensional acoustic reconstructions of thunder sources.

4.5. Interferometer Sensitivity

Both the interferometer and the LMA have minimum detectable powers, which are limited by environmental noise levels, approaching −90 to −95 dBm. Whereas the LMA stations utilize tuned VHF dipole antennas and power-detecting logarithmic amplifiers to measure the peak arrival times and received powers of impulsive events over a wide (100 dB) dynamic range, the interferometer receivers use less-sensitive flat plate antennas, linear amplifiers, and deep 16 bit fast digitizers to record the coherent raw time series data over a

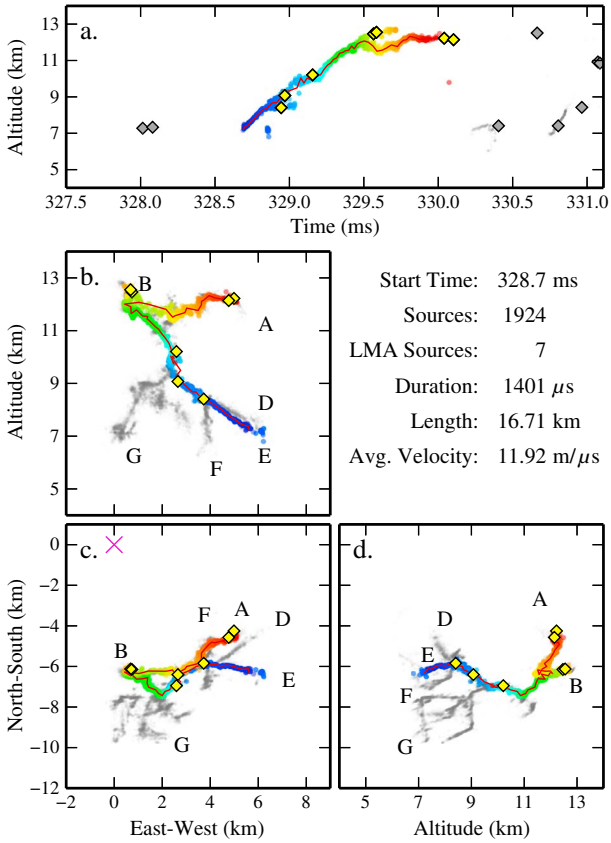

Figure 12. Quasi 3-D reconstruction of the extensive K-event of Figure 9, used to determine the propagation velocity of the upward negative leader. From a piecewise-linear fit to the observations (red line) and the high time resolution of the interferometer, the 3-D development of this and other flash activity can be examined in detail.

wide bandwidth. The increased bandwidth of the interferometer when compared to the LMA (20–80 MHz compared to 60–66 MHz) improves the sensitivity of the interferometer; however, the improvement offered by increased bandwidth is partially offset by the insensitive antenna design.

Because LMA networks are able to locate sources in three dimensions, the received power values can be used to determine the radiated power at the source [*Thomas et al.*, 2001, 2004] and correspond to the source power in dBW units (decibels relative to 1 W reference power) over the 6 MHz bandwidth of its measurements. On the other hand, a single network of interferometer receivers locates the source only in two dimensions and can determine only the received signal powers, either from the computed powers at each of the antennas or from the peak of the cross correlations between antenna pairs. The results are expressed as power levels at the receiver input, in dBm units (decibels relative to 1 mW reference power; 0 dBm = −30 dBW).

In this section we compare the interferometer and LMA observations to determine the relative sensitivities of the two systems. We begin by referring to the histograms of the powers for located radiation events from the two systems, shown in Figures 11e and 11j. Both are plotted over a 70 dB range of power values: −40 to −110 dBm received power values for the interferometer and −35 to +35 dBW source power for the LMA. From the width of the histograms, it is evident that the interferometer observations have a wider dynamic range than the LMA, with received powers varying from about −50 dBm down to −92 dBm for the interferometer, a 42 dB range of values, and the LMA-detected source powers varying between about +21 or +26 dBW down to −8 dBW, or over a range of 29–34 dB. If it is assumed that the highest power events are the same in both histograms, as shown by the light gray overlay in Figure 11e, it follows that the interferometer was 8–13 dB more sensitive than the LMA. Given that the minimum detectable source powers by the LMA for the flash were −8 dBW, the interferometer will have been detecting source powers down to about −16 to −21 dBW. The 5 dB uncertainty in this result is due to the uncertainty in correlating the maximum power levels of the two sets of measurements.

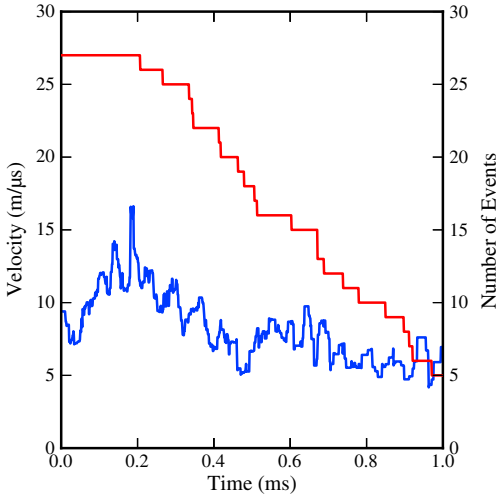

Figure 13. Average velocity versus time of 28 retrograde K-leaders (blue graph) over a 1 ms time interval, indicating an increase in the initial 200 μs of the leader, followed by a generally declining velocity. All but five of the leaders were less than 1 ms in duration (Table 2); the red graph shows the number of leaders whose duration was less than the indicated time steps and subsequently dropped out of the velocity determination.

A better way of determining the relative sensitivity is to identify the subset of interferometer located events that were time and space correlated with the LMA sources, and to compare the resulting sets of power values. This is done in Figure 14. Out of 1090 LMA sources, 640 were found to have high-quality, well-correlated interferometer observations. Only sources having a fractional multiplicity greater than 0.9, indicative of being impulsive in nature and well-isolated time-wise were considered for the correlation. The histogram of Figure 14b shows the difference in microseconds of the predicted arrival times of the LMA events at the interferometer site with the observed GPS-based arrival times. Almost all of the high multiplicity interferometer events occurred within ±1 μs of their predicted occurrence (red-dashed lines). Using ±1 μs as an acceptance criteria, Figure 14a shows a scatter diagram of the resulting sets of powers. The unity-slope green lines show a 10 dB spread in the data about a 1:1 correlation. Although the received interferometer powers ranged between −50 and −92 dBm, only events stronger than about −83 dBm on average were well-correlated with the LMA data.

The red-dashed line shows the result of offsetting and overlaying the power histograms as indicated in Figure 11e. The solid red line shows the offset determined by the average of the 640 correlated events. As seen in the histogram of Figure 11e, the minimum detected power of the interferometer events was about −92 dBm, shown as the dotted line in the scatterplot. From the intersection with the average offset (red) line, the minimum detected source power by the interferometer for the flash was about −19 dBW. Assuming the 10 dB scatter remained constant, the range of minimum detected source powers is indicated by the intersections of the green and dotted lines, and correspond to −15 to −25 dBW.

From the above, the interferometer observations show events whose source powers extend down to about −19 dBW, with +4 dB and −6 dB uncertainty. We note that sensitivities of −20 dBW and even down to −30 dBW (10 down to 1 mW in a 6 MHz bandwidth around 63 MHz) are routinely realized in LMA networks observations of overhead lightning activity and thus have sensitivities comparable to that of the interferometer. These sensitivity levels were not realized by minimal LMA network available at early season flash of this study but will have been realized in many other flashes observed by interferometer since then, which are the subject of ongoing study.

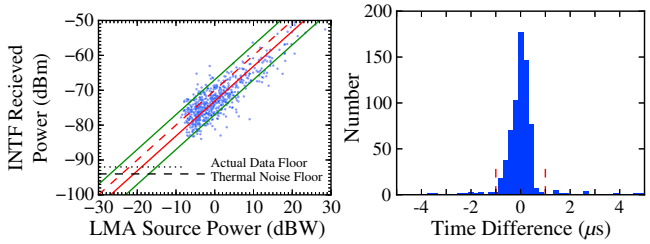

Figure 14. (left) Comparison of measured power values for the interferometer and LMA observations is used to estimate the sensitivity of the interferometer measurements (see text). (right) Only high-quality, impulsive interferometer sources that were well-correlated temporally and spatially with LMA events were used in estimating the sensitivity; almost all impulsive events were within 1 μs of each other. The green lines correspond to a 10 dB spread in the data values. The solid red line shows the mean value of the power offsets, whose intersection with the observed data floor of the interferometer indicates that the interferometer detected events having source powers down to about −20 dBW whereas the early season LMA network detected source of powers only down to about −8 dBW. The dashed red line indicates the result of estimating the offset value from the power histograms of Figure 11, which is less certain.

In the context of the present study, a primary reason for carefully determining the interferometer sensitivity concerns observations of triggered lightning reported in similar detail by *Edens et al.* [2012]. As discussed in the following section, the LMA data of that study (prior to development of the interferometer) showed clear evidence of radiation from upward positive breakdown from triggered lightning, whose source power values were between about −10 and −20 dBW. From this, we conclude that the interferometer observations were also seeing radiation directly associated with positive breakdown, as are LMA networks having the requisite sensitivity levels.

5. Discussion

The observations of this study show the development of lightning at VHF in exceptional detail. This is due in part to the interferometer being broadband, but for this study is primarily the result of being able to record the interferometer data continuously with time during a flash. The ability to continuously record the time series waveforms is primarily a technological advance, but one that provides a quantum leap in the ability to study lightning. Except for the series of studies with a continuously recording analog interferometer by *Rhodes et al.* [1994], *Mazur et al.* [1995], and *Shao et al.* [1995, 1996], studies of lightning discharge processes with digital interferometers have primarily needed to record an intermittent succession of short time windows (typically two to a few tens of microseconds in duration) due to limited digitizer memory. While dictated by technology limitations at the time, it required the recording to be triggered and the resulting observations to be primarily restricted to large-amplitude signals and to be greatly undersampled in time. Initial work with the interferometer of this study showed that its sequential triggering scheme produced observations similar to those of the LMA, but of generally lesser quality and in 2-D rather than 3-D.

The obvious advantage of continuous recording is that it allows the entire sequence of lightning activity to be observed, down and into background noise levels. In so doing, however, the effects of noise become much more prominent. Determining the location of sources having a high signal-to-noise ratios is relatively easy, and no special techniques are required. The same cannot be said for sources whose received amplitude is close to the background noise level. This has made it necessary to develop techniques to reduce the effects of noise and to distinguish between solutions contaminated by noise from those produced by lightning alone.

The advantages of broadband measurements are several fold: First, it reduces the number of antennas and receiving channels required for the measurements and eliminates the need to resolve fringe ambiguities of narrowband systems. Large fractional bandwidths are possible in the lower VHF, which takes advantage of the increased signal strength of the lightning radiation, thereby increasing the sensitivity of the measurements, while at the same time providing a wider range of baseline lengths for good angular uncertainty in the locations. Finally, the increased bandwidth improves the temporal resolution of the measurements by shortening the system response to impulsive events, enabling multiple impulsive events such as stepping to be separated from each other time-wise. As seen in Figure 2, the duration of the impulse response for a system of bandwidth B is 2–3 times 1/B, or 32–48 ns for the 60 MHz bandwidth of this study.

5.1. The Usefulness of LMA Data

Although extending interferometric techniques to obtain three-dimensional observations is possible in principle, there are substantial difficulties in doing so, both theoretical and practical. Except for the study by *Tantisattayakul et al.* [2005], most three-dimensional studies have utilized triangulation from the data of two or more interferometer stations to determine the source locations [e.g., *Mazur et al.*, 1995; *Defer et al.*, 2001; *Akita et al.*, 2010]. While the measurements at each station are coherent, the triangulation process itself is incoherent and results in spatially noisy images of the lightning activity. By contrast, time-of-arrival measurements such as those provided by the LMA receive the data incoherently at the stations (by measuring power rather than time series data) but combine the measurements coherently by means of accurate GPS time bases, resulting in superior spatial resolution.

As shown in the present study, it is not necessary for the interferometer observations themselves to be 3-D; rather two-dimensional measurements from a single station can be successfully combined with 3-D TOA/LMA observations to produce good quality quasi 3-D images having the high time resolution and detail of the interferometer data. Similar quasi 3-D reconstructions of broadband interferometer observations have been used by *Qiu et al.* [2012] to determine leader velocities of CG discharges, based on

three-dimensional acoustic measurements of thunder. When and where available, TOA observations will necessarily give substantially better 3-D renditions.

Regardless of whether quasi 3-D constructions are made, the interferometer and LMA observations valuably complement each other. The LMA accurately locates and characterizes impulsive lightning events, while the interferometer is able to locate and image both continuously radiating and impulsive events, with lesser spatial resolution but a much improved timing resolution. Although the LMA is capable of obtaining source locations in successive 10 μs time windows, locatable impulsive events are not produced this often by continually radiating events, or the continuous events do not last long enough to be adequately characterized. The difference is clearly seen in the comparisons of Figure 9. At the same time, however, the LMA data valuably complement the interferometer observations by explicitly identifying impulsive events and putting the interferometer observations in a three-dimensional context.

The interferometer and LMA observations for the lightning activity agree exceptionally well, as seen, for example, in Figures 9a and 9b. The initial results confirm the complementary nature of the two sets of observations and valuably extend the ability to interpret and more fully understand the observations. The understanding will be further improved by inclusion of fast electric change measurements of lightning currents and electrostatic field change measurements of charge transfer, now in process. Comparing the various observations in the 2-D context of the interferometer is quite sufficient, given that the basic 3-D structure is known from the LMA data.

5.2. K-Events and Positive Breakdown

An important issue in studying lightning processes has been determining the manner in which positive breakdown processes develop within negative charge regions inside a storm. The results of this study expand our understanding of K-processes and the role they play in keeping the positive channels alive and conducting. The K-process consists of a retrograde negative leader often being initiated at a distance behind the advancing tip of previously detected activity, and noisily propagating back along the channel to an apparently more conducting primary channel, where the radiation either continues, becomes weaker, or ceases as the leader continues propagating into and further along the channel. Upon joining a primary channel, a strong burst of radiation sometimes occurs, indicating that the two channels had different electric potentials, and implying that the channel traversed by the leader up to that point had decayed to a nonconducting state by the time of the K-event. Many or most of the negative K-leaders of this study likely continue up along part or the full length of the main channels, rejuvenating or strengthening them in the process. The effect of successive K-events likely kept negative charge flowing toward and into the upper positive charge regions, as found from charge transfer studies of IC flashes [e.g., *Krehbiel*, 1981]. The charge transfer is often insufficient to keep the negative channels extending through virgin air in the positive charge region, however, as indicated, for example, by extended VHF-quiet intervals in the upper level negative breakdown of the IC flash in this study. The K-activity of intracloud flashes is identically the same as that observed in the interstroke and prestroke intervals of negative cloud-to-ground flashes, both of which are produced by the same positive breakdown processes within the negative charge region. The retrograde negative leader becomes a downward dartleader in CG discharges and an upward K-leader in normal polarity IC flashes. The retrograde negative breakdown is also the same as that seen optically by high-speed video recordings during the progression of positive leaders to ground [*Saba et al.*, 2008; *Warner*, 2011], which provided important clues as to the nature of in-cloud positive breakdown. In all cases, the activity occurs intermittently and repeatedly, and in a retrograde manner.

In addition to the retrograde breakdown, the results of this study suggest that K-events appear to produce non-VHF radiating forward-directed potential waves, either upon initiation or upon contact of the retrograde leader with a conducting channel. In the latter case, the forward wave appears to be the cause a strong burst of VHF radiation upon reaching the tip of previously detected activity. A better understanding of this phenomena awaits further study.

In addition to K-events, the interferometer observations provide an intriguing glimpse into other aspects of the positive breakdown. A particular question in this regard is whether VHF radiation is produced and being detected from the optically and energetically faint positive leaders. The interferometer observations show the occurrence of a steady but somewhat random sequence of what we have termed "flickering" VHF activity, which accumulates over time and space to reveal the developing positive channels. The flickering sources are also seen at the furthest extent of the positive leader as it propagates into the main negative

charge region. These faint sources appear qualitatively different from the emission seen in brief negative K-leaders and also from the larger scale flickers seen in the positive leader body. However, the VHF waveforms produced in the positive breakdown region of the flash show that the emission is impulsive, rather than continuous as would be expected of virgin positive breakdown.

We attribute the above activity as being due to an unknown feature of the positive breakdown itself. This is supported by a detailed study of upward positive breakdown during a triggered lightning discharge by *Edens et al.* [2012], which showed about as convincingly as possible VHF radiation produced by the upward-developing positive breakdown that initiated the triggering. As shown in Figure 3 of Edens' study, the LMA-detected sources of the upward positive breakdown had VHF source powers between −10 to −20 dBW. The Langmuir LMA was not yet fully operational at the time of the 2012 observations discussed here. As a consequence, the LMA was less sensitive than usual, with minimum detectable source powers of only about −8 dBW for the flash being studied. However, from the detailed analysis in section 4.5, the broadband interferometer was sufficiently sensitive to detect radiation events down to about −20 dBW, and hence the same kind of activity seen in the upward positive breakdown in the triggered lightning observations. This, along with the overall spatial development of the flickering sources, leads us to attribute them as being due in some way to the positive breakdown itself. More detailed study of the positive breakdown region of IC and hybrid CG flashes is underway with improved sensitivity of both the interferometer and LMA to provide more conclusive answers to the questions raised by the above observations.

Finally, more strongly radiating positive breakdown sometimes appeared to occur directed away from the developing tip of the positive breakdown, either as a fast leader and/or as isolated impulsive events at a distance beyond the previously detected tip. Examples of strongly radiating fast positive leaders were observed by *Shao et al.* [1995] immediately following −CG strokes in Florida storms.

5.3. Interferometry and Imaging

As is the case for other lightning interferometer studies, the interferometer of the present study is operated as a short-baseline time-of-arrival system for determining the directions of the source centroids. Describing such systems also as interferometers is fully appropriate, however, because of the coherent nature of the measurements and the manner in which the data are processed, involving multiple pairs of receiving antennas. For narrowband systems, the phase difference between pairs of antenna signals is measured, from which the time delay and arrival direction is obtained—the classic interferometer technique. Multiple baseline lengths are required to obtain the desired angular resolution, but which have fringe ambiguities that need to be resolved.

For broadband systems, the time delay can be determined by computing the cross spectra for each pair of antennas and obtaining the time delays either from the slope of the phase difference versus frequency [e.g., *Kawasaki et al.*, 2000; M. Akita et al., submitted manuscript, 2013] or, more simply and better, by transforming the cross spectrum back into the time domain to obtain the cross-correlation function, whose peak is the time delay. Either way, the broadband approach has the substantial advantage over narrowband measurements of not requiring physically different baseline lengths. In effect, a continuum of baseline lengths in terms of wavelengths is obtained for each pair of antennas without having to resolve fringe ambiguities.

In further support of narrow or broadband systems being interferometers, and looking forward to future advances in their use for studying lightning, we note that, by simply changing the processing algorithm, the same data can be used produce actual images of the radiation activity of multiple or distributed sources within each (1.42 μs) time window. The basis for doing this are the fundamental ideas of Fourier optics. Namely that the image of a two-dimensional pattern of radiation sources is the Fourier transform of the diffraction pattern of the sources incident upon the observer. At optical frequencies, the Fourier transformation is produced by the eye or other lenses. At radio frequencies, the incident diffraction pattern is sampled by an array of antennas, the Fourier transform of which is the source image in the direction cosine plane.

Techniques for obtaining images have been fully developed and applied by the radio astronomy community, utilizing large arrays of receiving antennas [*Taylor et al.*, 1999]. Correlations between all possible pairs of antennas sample the diffraction pattern over a variety of baseline lengths and directions, which is related to the radio image in the sky by a two-dimensional Fourier transformation. For narrowband systems, a general baseline corresponds to a single location in the spatial frequency or u,v diffraction plane, namely $u = d_x/\lambda$ and $v = d_y/\lambda$, where d_x and d_y are the displacements between the two antennas in the x and y directions,

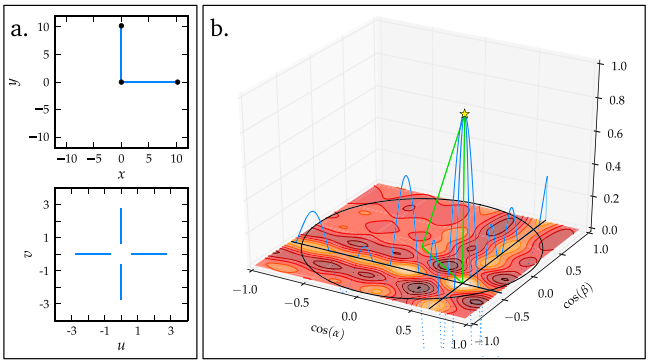

Figure 15. Example illustrating how the broadband data can be used to instantaneously image the lightning activity within a given 1.42 μs time window, as opposed to locating only the strongest source. The blue lines extending both above and below the direction cosine plane are the cross-correlation results from each orthogonal baseline, whose peak intersection (yellow star) is the centroid of the strongest source. The radiation intensity can be determined over the entire direction cosine plane, as indicated by the diffraction pattern associated with a minimal three-antenna array.

and the baseline length between the antennas is $d = \sqrt{d_x^2 + d_y^2}$. Many sets of antennas and baselines are required to sample the diffraction pattern sufficiently to produce a quality image. For broadband systems, data from a given pair of antennas correspond to a range of baseline distances in terms of wavelengths, greatly increasing the extent to which the diffraction pattern is sampled. As result, broadband systems can produce quality images with fewer antennas.

An example of a simple image from the data of this study is shown in Figure 15. In this case the data are from a 256 sample window of the interferometer record (the same window shown in Figure 2), corresponding to a time interval of 1.42 μs. For the interferometer of this study, the baselines vary from $(2/3)\lambda$ to $(8/3)\lambda$, namely by a factor of 4. The antenna locations in the *x*,*y* measurement plane are shown in Figure 15a along with the corresponding sampling in terms of wavelengths in the *u*,*v* plane. The third baseline, corresponding to the diagonally displaced outlying antennas, has been omitted to simplify the figure but could be used to further improve the sampling. The one-dimensional cross correlation obtained from the cross spectrum of each baseline corresponds to the image values in orthogonal directions in the direction cosine plane (blue lines in Figure 15b). The intersection of the correlation peaks corresponds to the centroid value obtained in the present study.

To obtain a full image, a two-dimensional transformation is applied to the sampled *u*,*v* cross spectra. The result is shown in the direction cosine plane as the colored contour patterns (Figure 15b). In this case there was a single localized source, and the image is dominated by the source and a rectangular grid of sidelobes associated with the cross-correlation oscillations. The sidelobes are stronger in the $\cos(\alpha)$ or north-south baseline than in the east-west baseline, due to a correlated interference source being detected by each of its antennas (but not by the third antenna). The amplitude of the sidelobes reduces with the inclusion of additional baselines. The angular resolution of the image is improved by sampling the diffraction pattern at higher *u*,*v* values (corresponding to higher spatial frequencies), obtained through the use of longer baselines or higher measurement frequencies.

In conclusion, the continuous recording interferometer is still evolving as an instrument. For the 2013 season, the antenna and front-end design was improved to increase the system sensitivity, and a fourth antenna was added to develop suitable techniques for combining multiple, nonorthogonal baselines. Numerous observations have been obtained of a variety of lightning types, including overhead intracloud flashes for studying positive breakdown processes, bolt-from-the-blue flashes for which the positive and negative breakdown processes are horizontally separated, and observations of several close, energetic narrow bipolar events.

Appendix A: Noise Reduction

When the interferometer time series waveforms are recorded down into the noise levels and continuously with time, numerous sources are produced that are partially or entirely due to or affected by noise.

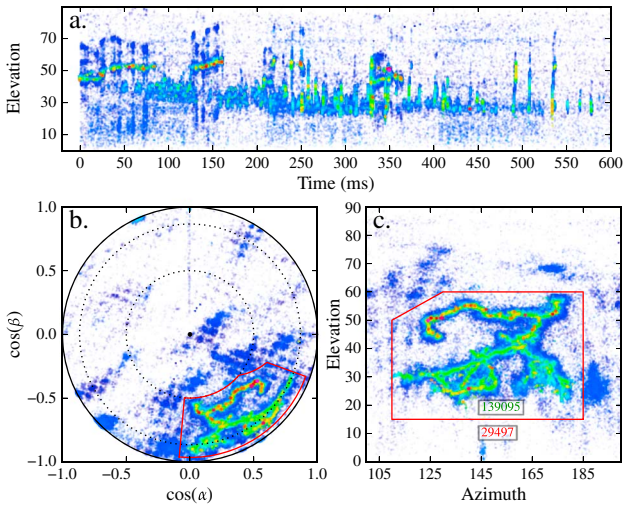

Figure A1. Raw interferometer data prior to any metric filtering, showing the noisiness of the observations resulting from the data recording being continuous and extending into the ambient receiver noise levels. The results are to be compared with the cleaned-up data of Figures 5 and 6. The red trapezoid coarsely divides azimuth and elevation space into exterior and interior regions containing, respectively, (i) noise-only events and (ii) lightning and noise-contaminated events. The rectangular boxes indicate the number of sources within each region, and the source colors represent received power values.

A robust noise reduction technique is therefore critical to the full utilization of the data. Noise effects are not as important when the data are acquired as a series of short-duration windows using amplitude-based triggering, as the results are dominated by the triggering event.

Figure A1 illustrates the various noise effects in the data, while Figures A2 and A3 show how the effects are ameliorated by the metric filtering developed in this study. In each case the sources shown both for the entire sky (Figures A1a, A2a, A3a, A1b, A2b, and A3b) and over a limited azimuth and elevation range that includes the lightning flash (Figures A1c, A2c, and A3c). To assist in identifying noise sources, the azimuth-elevation results are coarsely partitioned into two regions by the red trapezoidal box, in which the exterior sources are noise-only produced.

A1. Phase 0: No Noise Reduction

Figure A1 shows the observations before any noise effects have been removed. The flash is well identified by its high-amplitude sources, but the lower-amplitude sources are affected and blurred by noise. The noise falls predominately into two categories, most clearly seen in the direction cosine projection: small clusters of points that lie on a fine grid, and large parallel stripes of clusters running in the ENE direction. The grid of sources is a byproduct of aliasin [*Moddemeijer*, 1991]. Any signal outside the Nyquist band that is not attenuated by the bandpass filtering or that is introduced subsequent to the filtering causes the sources to bunch into clusters, including the lightning sources themselves. The grid spacing is determined by time differences which are integer multiples of the sampling period. If the lightning signal is not band limited, their locations fall on the same grid. The larger-scale parallel ENE structures are produced by in-band radio interference being picked up by two receiving antennas close to the instrument trailer during 2012. The interference caused the cross correlation of the two channels to ring excessively, with each peak of the ringing producing one of the parallel structures. This noise effect also contaminated weak lightning sources and moved them into the parallel smear, as can be seen in Figure A1a sources above the initial negative leader activity.

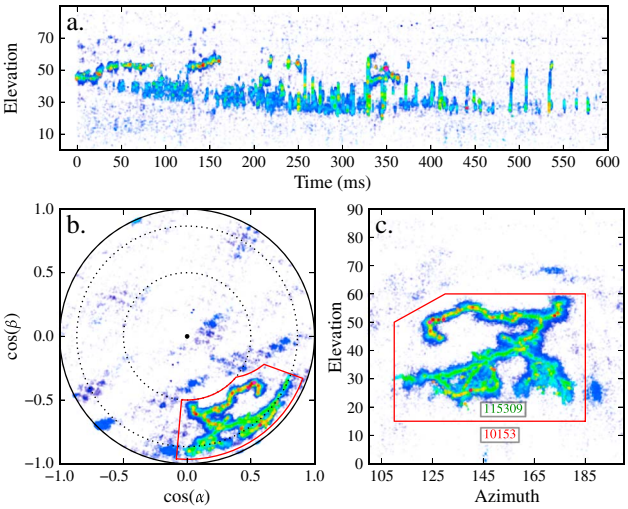

Figure A2. Same as Figure A1 but after Phase 1 metric-based noise reduction has been applied. Two thirds of the noise-only sources have been removed, but a number of noise-contaminated or noise-only sources remain inside the flash region.

A2. Phase 1: Noise Reduction

Figure A2 shows the results after the first noise reduction phase, based on closure delay and standard deviation.

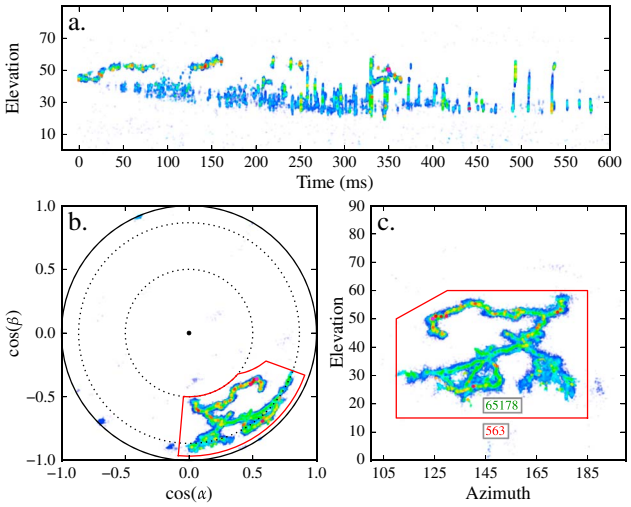

Figure A3. Same as Figure A2 but after strong Phase 2 noise reduction has also been applied. Nearly all noise sources have been removed, but the total number of sources inside the flash box has also been reduced by a factor of 1/2.

The closure delay metric identifies sources with phase ambiguities, and the standard deviation identifies multi-source locations and chance correlations. The noise reduction in this phase is relatively mild in that the solutions removed are almost exclusively noise damaged. This can be seen in the number of solutions inside and outside the flash region, which is reduced heavily outside but not inside the red box.

Even though the phase 1 noise reduction is relatively mild, it removes a majority of the noise sources. In the case that the interferometer is located in an area with few correlated noise sources, phase 1 reduction is all that is needed to clean the map. However, VHF noise is pervasive and quiet locations are uncommon.

A3. Phase 2: Noise Reduction

Figure A3 shows the results after the second noise reduction phase, based on multiplicity and correlation amplitude. Multiplicity, defined in section 3.2, is a measure of how isolated a source is time-wise. Correlation amplitude is a measure of the signal-to-noise ratio and is the metric most related to signal amplitude. The noise reduction is much more severe in this phase; while noise sources are almost completely removed, many well-determined weak lightning sources are also removed. As such, the decision threshold for phase 2 noise reduction is much more subjective. The results presented in this paper use a relatively extreme threshold to heavily reduce noise at the expense of correct low-power lightning solutions. As a result, almost no noise sources are left in the region outside the red box.

Acknowledgments

This research was supported by the Defense Advanced Research Projects Agency under grant HR0011-10-1-0059 and by the National Science Foundation under grants AGS-1205727 and ATM-0536950. Previous equipment support was provided by the U.S. Missile Defense Agency under grant HQ0147-08-C-0025. The authors thank Sanjay Bhatnagar and David Meier for discussion of the general interferometer technique, the reviewers for their constructive comments, and the Associate Editor, Ted Mansell, for additional comments and guiding the paper through the review process. The data used for this study are available upon request to Langmuir Laboratory, langmuir.nmt.edu.

References

Akita, M., Y. Nakamura, S. Yoshida, T. Morimoto, T. Ushio, Z. Kawasaki, and D. Wang (2010), What occurs in K process of cloud flashes?, *J. Geophys. Res.*, *115*, D07106, doi:10.1029/2009JD012016.

Azaria, M., and D. Hertz (1984), Time delay estimation by generalized cross correlation methods, *IEEE Trans. Acoust. Speech Signal Process.*, *32*(2), 280–285.

Behnke, S. A., R. J. Thomas, P. R. Krehbiel, and W. Rison (2005), Initial leader velocities during intracloud lightning: Possible evidence for a runaway breakdown effect, *J. Geophys. Res.*, *110*, D10207, doi:10.1029/2004JD005312.

Bondiou, A., I. Taudière, P. Richard, and F. Helloco (1990), Analyse spatio-temporelle du rayonnement VHF-UHF associé à l'éclair, *Rev. Phys. Appl.*, *25*(2), 147–157.

Boucher, R., and J. Hassab (1981), Analysis of discrete implementation of generalized cross correlator, *IEEE Trans. Acoust. Speech Signal Process.*, *29*(3), 609–611.

Cao, D., X. Qie, S. Duan, J. Yang, and Y. Xuan (2010), Observations of VHF source radiated by lightning using short baseline technology, in *2010 Asia-Pacific Symposium on Electromagnetic Compatibility (APEMC)*, pp. 1162–1165, IEEE, Beijing, China.

Carter, G. (1987), Coherence and time delay estimation, *Proc. IEEE*, *75*(2), 236–255.

Cummins, K. L., M. J. Murphy, E. A. Bardo, W. L. Hiscox, R. B. Pyle, and A. E. Pifer (1998), A combined TOA/MDF technology upgrade of the U.S. National Lightning Detection Network, *J. Geophys. Res.*, *103*(D8), 9035–9044.

Defer, E., P. Blanchet, C. Théry, P. Laroche, J. E. Dye, M. Venticinque, and K. L. Cummins (2001), Lightning activity for the July 10, 1996, storm during the stratosphere-troposphere experiment: Radiation, Aerosol, and Ozone-A (STERAO-A) experiment, *J. Geophys. Res.*, *106*(D10), 10,151–10,172.

Edens, H., et al. (2012), VHF lightning mapping observations of a triggered lightning flash, *Geophys. Res. Lett.*, *39*, L19807, doi:10.1029/2012GL053666.

Hassab, J., and R. Boucher (1979), Optimum estimation of time delay by a generalized correlator, *IEEE Trans. Acoust. Speech Signal Process.*, *27*(4), 373–380.

Hayenga, C. (1984), Characteristics of lightning VHF radiation near the time of return strokes, *J. Geophys. Res.*, *89*(D1), 1403–1410.

Jacovitti, G., and G. Scarano (1993), Discrete time techniques for time delay estimation, *IEEE Trans. Signal Process.*, *41*(2), 525–533.

Kawasaki, Z., R. Mardiana, and T. Ushio (2000), Broadband and narrowband RF interferometers for lightning observations, *Geophys. Res. Lett.*, *27*(19), 3189–3192.

Krehbiel, P. (1981), An analysis of the electric field change produced by lightning, PhD thesis, University of Manchester Institute of Science and Technology.

Maier, L., C. Lennon, T. Britt, and S. Schaefer (1995), LDAR system performance and analysis, paper presented at International Conference on Cloud Physics, Dallas, Tex.

Mazur, V., P. R. Krehbiel, and X.-M. Shao (1995), Correlated high-speed video and radio interferometric observations of a cloud-to-ground lightning flash, *J. Geophys. Res.*, *100*(D12), 25,731–25,753.
Moddemeijer, R. (1991), On the determination of the position of extrema of sampled correlators, *IEEE Trans. Signal Process.*, *39*(1), 216–219.
Proctor, D. (1981), VHF radio pictures of cloud flashes, *J. Geophys. Res.*, *86*(C5), 4041–4071.
Qiu, S., B. Zhou, L. Shi, W. Dong, Y. Zhang, and T. Gao (2009), An improved method for broadband interferometric lightning location using wavelet transforms, *J. Geophys. Res.*, *114*, D18211, doi:10.1029/2008JD011655.
Qiu, S., B.-H. Zhou, and L.-H. Shi (2012), Synchronized observations of cloud-to-ground lightning using VHF broadband interferometer and acoustic arrays, *J. Geophys. Res.*, *117*, D19204, doi:10.1029/2012JD018542.
Rhodes, C., X. Shao, P. Krehbiel, R. Thomas, and C. Hayenga (1994), Observations of lightning phenomena using radio interferometry, *J. Geophys. Res.*, *99*(D6), 13,059–13,082.
Richard, P., A. Delannoy, G. Labaune, and P. Laroche (1986), Results of spatial and temporal characterization of the VHF-UHF radiation of lightning, *J. Geophys. Res.*, *91*(D1), 1248–1260.
Rison, W., R. Thomas, P. Krehbiel, T. Hamlin, and J. Harlin (1999), A GPS-based three-dimensional lightning mapping, *Geophys. Res. Lett.*, *26*(23), 3573–3576.
Saba, M. M., K. L. Cummins, T. A. Warner, E. P. Krider, L. Z. Campos, M. G. Ballarotti, O. Pinto, and S. A. Fleenor (2008), Positive leader characteristics from high-speed video observations, *Geophys. Res. Lett.*, *35*, L07802, doi:10.1029/2007GL033000.
Schultz, C. J., W. A. Petersen, and L. D. Carey (2011), Lightning and severe weather: A comparison between total and cloud-to-ground lightning trends, *Weather Forecast.*, *26*(5), 744–755.
Shao, X., and P. Krehbiel (1996), The spatial and temporal development of intracloud lightning, *J. Geophys. Res.*, *101*(D21), 26,641–26,668.
Shao, X., P. Krehbiel, R. Thomas, and W. Rison (1995), Radio interferometric observations of cloud-to-ground lightning phenomena in Florida, *J. Geophys. Res.*, *100*(D2), 2749–2783.
Shao, X., D. Holden, and C. Rhodes (1996), Broad band radio interferometry for lightning observations, *Geophys. Res. Lett.*, *23*(15), 1917–1920.
Shao, X.-M. (1993), The development and structure of lightning discharges observed by VHF radio interferometer, PhD thesis, New Mexico Institute of Mining and Technology.
Sun, Z., X. Qie, M. Liu, D. Cao, and D. Wang (2012), Lightning VHF radiation location system based on short-baseline TDOA technique–Validation in rocket-triggered lightning, *Atmos. Res.*, *129*, 58–66.
Tantisattayakul, T., K. Masugata, I. Kitamura, and K. Kontani (2005), Broadband VHF sources locating system using arrival-time differences for mapping of lightning discharge process, *J. Atmos. Sol. Terr. Phys.*, *67*(11), 1031–1039.
Taylor, G. B., C. L. Carilli, and R. A. Perley (Eds.) (1999), *Synthesis Imaging in Radio Astronomy II*, vol. 180, Astronomical Society of the Pacific, San Francisco, Calif.
Thomas, R., P. Krehbiel, W. Rison, T. Hamlin, J. Harlin, and D. Shown (2001), Observations of VHF source powers radiated by lightning, *Geophys. Res. Lett.*, *28*(1), 143–146.
Thomas, R., P. Krehbiel, W. Rison, S. Hunyady, W. Winn, T. Hamlin, and J. Harlin (2004), Accuracy of the lightning mapping array, *J. Geophys. Res.*, *109*, D14207, doi:10.1029/2004JD004549.
Ushio, T., Z. Kawasaki, Y. Ohta, and K. Matsuura (1997), Broadband interferometric measurement of rocket triggered lightning in Japan, *Geophys. Res. Lett.*, *24*(22), 2769–2772.
Warner, T. A. (2011), Observations of simultaneous upward lightning leaders from multiple tall structures, *Atmos. Res.*, *117*, 45–54.
Warner, T. A., M. M. F. Saba, R. E. Orville, K. L. Cummins, and W. A. Lyons (2013), Differences in positive and negative lightning leader appearance and behavior as observed by high-speed cameras, paper presented at Sixth Conference on the Meteorological Applications of Lightning Data, Austin, Tex.
Warwick, J. W., C. O. Hayenga, and J. W. Brosnahan (1979), Interferometric directions of lightning sources at 34 MHz, *J. Geophys. Res.*, *84*(C5), 2457–2468.